

Interplay between dressed and strong-axial-field states in Nitrogen-Vacancy centers for quantum sensing and computation

G. Zanelli^{1,2}, E. Moreva¹, E. Bernardi^{1*}, E. Losero¹, S. Ditalia Tchernij^{2,3},
J. Forneris^{2,3}, Ž. Pastuović⁴, P. Traina¹, I. P. Degiovanni¹, M. Genovese^{1,3}.

¹*Istituto Nazionale di Ricerca Metrologica (INRiM), Strada delle cacce 91, Turin, Italy*

²*Physics Department and NIS Centre of Excellence - University of Torino, Torino, Italy*

³*Istituto Nazionale di Fisica Nucleare (INFN) Sez. Torino, Torino, Italy and*

⁴*Centre for Accelerator Science, Australian Nuclear Science and Technology Organisation, New Illawarra rd., Lucas Heights, NSW 2234, Australia**

The Nitrogen-Vacancy (NV) center in diamond is an intriguing electronic spin system with applications in quantum radiometry, sensing and computation. In those experiments, a bias magnetic field is commonly applied along the NV symmetry axis to eliminate the triplet ground state manifold's degeneracy ($S=1$). In this configuration, the eigenvectors of the NV spin's projection along its axis are called strong-axial field states. Conversely, in some experiments a weak magnetic field is applied orthogonal to the NV symmetry axis, leading to eigenstates that are balanced linear superpositions of strong-axial field states, referred to as dressed states. The latter are sensitive to environmental magnetic noise at the second order, allowing to perform magnetic field protected measurements while providing increased coherence times. However, if a small axial magnetic field is added in this regime, the linear superposition of strong-axial field states becomes unbalanced. This paper presents a comprehensive study of Free Induction Decay (FID) measurements performed on a NV center ensemble in the presence of strain and weak orthogonal magnetic field, as a function of a small magnetic field applied along the NV symmetry axis. The simultaneous detection of dressed states and unbalanced superpositions of strong-axial field states in a single FID measurement is shown, gaining insight about coherence time, nuclear spin and the interplay between temperature and magnetic field sensitivity. The discussion concludes by describing how the simultaneous presence of magnetically-sensitive and -insensitive states opens up appealing possibilities for both sensing and quantum computation applications.

I. INTRODUCTION

The use of quantum states to sense physical observables, known as quantum sensing [1, 2], has demonstrated to be of factual advancement in a plethora of diverse applications (spanning from magnetometry, gravitational wave detection and quantum thermodynamics)[3–12]. However, isolating a sensor from different sources of noise represents a major challenge in high precision quantum sensing. Among several classes of quantum sensors, the Nitrogen-Vacancy (NV) center in diamond has been extensively studied as a high-sensitivity nanoscale sensor. More precisely, the NV is an optically active point defect composed of a single substitutional Nitrogen and a lattice vacancy in nearest-neighbour configuration; this structure leads to an electronic spin triplet configuration $S=1$ which can be exploited via spin resonance techniques allowing for the so-called Optically Detected Magnetic Resonance (ODMR)[13] (for an introductory description of NV levels structure and ODMR principle see [14]). NV-based sensing is commonly carried out by monitoring the effect of environmental variables on the dynamics of the NV center, this scheme is enabled by three main features [15]: (i) the spin state can be controlled using microwave radiation; (ii) the readout can be performed optically; (iii) the system presents coherence times T_2^* in the order

of tens of microseconds at room temperature[14, 16]. Various techniques have been introduced to make measurements selective on single physical observables, i.e. temperature or magnetic field. For example, thermal echo [17], D-Ramsey pulse sequences [18], quantum beats magnetometry [19], multipulse dynamical decoupling [20] and spectral hole burning [21] have been explored. Nonetheless, as it will be detailed, each environmental parameter may act differently depending on the quantum state of the NV center, thus a thorough analysis of the competition of these parameters in the involved physical process is required. This study will focus on Continuous-wave (CW) and Free Induction Decay (FID) sensing protocols; cw-sensing protocols aim to detect the variation induced on by external fields on the resonance frequency of the NV center. Free Induction Decay sensing protocols measure the phase difference acquired as a consequence of variation in resonance frequency between two components of a quantum superposition. Sensors based on NV centers present a very good sensitivity regarding temperature and magnetic field [22], leading to the possibility of measuring the temperature inside a cell [23–25], magnetic NMR signal coming from a single molecule [26, 27] as well as nanoscale imaging of superconducting vortexes [28]. Additionally, the NV is widely used in computation applications where paramagnetic ^{13}C nuclei are employed as q-bits, the NV center as a mediator q-bit, and the neighboring N nucleus as auxiliary q-bit [29, 30]. Moreover, In recent applications, the possibility of using

* e.bernardi@inrim.it

the network of ^{13}C nuclei for quantum simulation has been investigated [31].

In most of these applications, a bias magnetic field B_{\parallel} is applied along the NV axis to remove the degeneration of the $S_z = \pm 1$ manifold. In this case, the eigenstates of the system are NV's axial spin eigenstates, namely $|S_z = +1\rangle$ and $|S_z = -1\rangle$, generally indicated as strong-axial field states. Conversely, in the presence of a weak magnetic field, electric field or strain (or a combination) orthogonal to the NV axis (with $B_{\parallel} = 0$), the eigenstates are balanced linear superposition of the strong-axial field states: $|+\rangle = \frac{1}{\sqrt{2}}(|S_z = +1\rangle + |S_z = -1\rangle)$ and $|-\rangle = \frac{1}{\sqrt{2}}(|S_z = +1\rangle - |S_z = -1\rangle)$, typically called dressed states [13].

Dressed states have proven to be useful for temperature [32] and electric field measurements [33] since these states show a second order dependency to magnetic field due to the null spin expectation value for each direction: $\langle +|S_i|+\rangle = \langle -|S_i|-\rangle = 0$ for $i = x, y, z$, leading to longer coherence times [34] when the dominant source of decoherence is magnetic noise [35].

Dressed states have been studied both for single NV center [35–37] and NV ensemble [33, 34, 38, 39]. In the last few years, research has been focusing on the effect of ^{14}N [38] and ^{13}C [37] nuclei on the NV center and their exploitation for electrical field sensing [33, 40]. In particular, in the presence of a weak orthogonal field ($B_{\perp} \neq 0$, $B_{\parallel} = 0$), it has been shown that two resonances are present for both $|-\rangle$ and $|+\rangle$ [38]. The first is related to the state $I_z^{14\text{N}} = 0$, and the other is related to the two degenerate states $I_z^{14\text{N}} = \pm 1$, where $I_z^{14\text{N}}$ is the component of the ^{14}N nuclear spin along the NV axis. This result proves that the NV center interacts with the ^{14}N nucleus, despite being almost insensitive to external magnetic fields. The reason is that (for $B_{\parallel} = 0$) the state with $I_z^{14\text{N}} = 0$ is a balanced superposition of strong-axial field states, therefore it is a completely dressed state. The states with $I_z^{14\text{N}} = +1$ and $I_z^{14\text{N}} = -1$, instead, are unbalanced superpositions of the strong-axial-field states with $\langle S_z \rangle > 0$ and $\langle S_z \rangle < 0$ respectively, as a result they are more sensitive to the external magnetic field. In this work, these unbalanced superpositions of $|S_z = +1\rangle$ and $|S_z = -1\rangle$ are named partially-dressed states. Finally, it should be stressed that that it is not necessary to apply a weak orthogonal field to observe the interaction between dressed and partially dressed states in the FID decays. The total electric field alone has a similar effect on the eigenenergies of a single NV [41] and is likely to have similar effects on the FID decays. However, employing a weak orthogonal field can enhance the stability of the dressed states by increasing the energy gap, when properly aligned. Additionally, it eliminates the overlap of resonances associated with different orientations of NV's when working with NVs ensembles.

In this paper, via a comprehensive theoretical and experimental investigation of the interplay between dressed and strong-axial field states in the presence of both a weak

orthogonal magnetic field and an electric field (or, equivalently, a strain), it is demonstrated for the first time the possibility of simultaneously exciting dressed and partially-dressed states, together with a novel approach consisting of fitting single FID measurements with multiple coherence times, that is of critical importance when working with different classes of states. This methodology will lead the implementation of two-qubit gates with an increased fidelity due to the increased coherence time T_2^* of dressed and partially-dressed states. Moreover, it could enable a decoupled magnetic field and temperature sensing scheme, operating with limited microwave bandwidth and with a single microwave frequency. In the first part of the work, it is discussed how strain and weak orthogonal field compete in forming dressed states, providing, as a result, the exact eigenstates of the system. Then, FID measurements obtained for two different values of axial magnetic field are presented, highlighting the presence of dressed and partially-dressed states, exploiting a suitable diamond sample. The study is focused to NV ensembles, but it can be straightforwardly generalized to the single NV center or other solid-state spin systems.

II. THEORETICAL ANALYSIS

The system considered is constituted of NV center electronic spin $\vec{S} = 1$ and ^{14}N nuclear spin $\vec{I} = 1$. The complete Hamiltonian of this system is [13]:

$$\begin{aligned} \mathcal{H} = & (D_{gs} + d_{\parallel}\Pi_{\parallel}) \left[S_z^2 - \frac{1}{3}S(S+1) \right] \\ & - d_{\perp} [\Pi_x(S_x^2 - S_y^2) - \Pi_y(S_xS_y + S_yS_x)] \\ & + g_e\mu_B B_x S_x + g\mu_B B_y S_y \\ & + g_e\mu_B B_{\parallel} S_z \\ & + S_z A_{\parallel} I_z + S_x A_{\perp} I_x + S_y A_{\perp} I_y \\ & + Q \left(I_z^2 - \frac{I^2}{3} \right) \\ & + g_n\mu_n B_x I_x + g_n\mu_n B_y I_y \\ & + g_n\mu_n B_{\parallel} I_z, \end{aligned} \quad (1)$$

where D_{gs} is the ground state Zero Field splitting, d_{\perp} and d_{\parallel} are the components of the ground state electric dipole moment, $\vec{\Pi} = \vec{E} + \vec{\sigma}$ is the total effective electric field that includes both the effect of static electric fields \vec{E} and strain $\vec{\sigma}$ (strain acts as an effective electric field due to the piezoelectric effect). g_e and g_n are electric and nuclear Landé g factors, μ_B and μ_n are the Bohr and nuclear magneton constant, \vec{B} is the applied magnetic field, A_{\parallel} and A_{\perp} describe the hyperfine interaction between S and I , and Q is the nuclear electric quadrupole term.

In Fig. 1 (a), the eigenvalues of Hamiltonian [42] in Eq. 1 are numerically evaluated in the presence of a weak fixed orthogonal field \vec{B}_{\perp} and plotted functions of

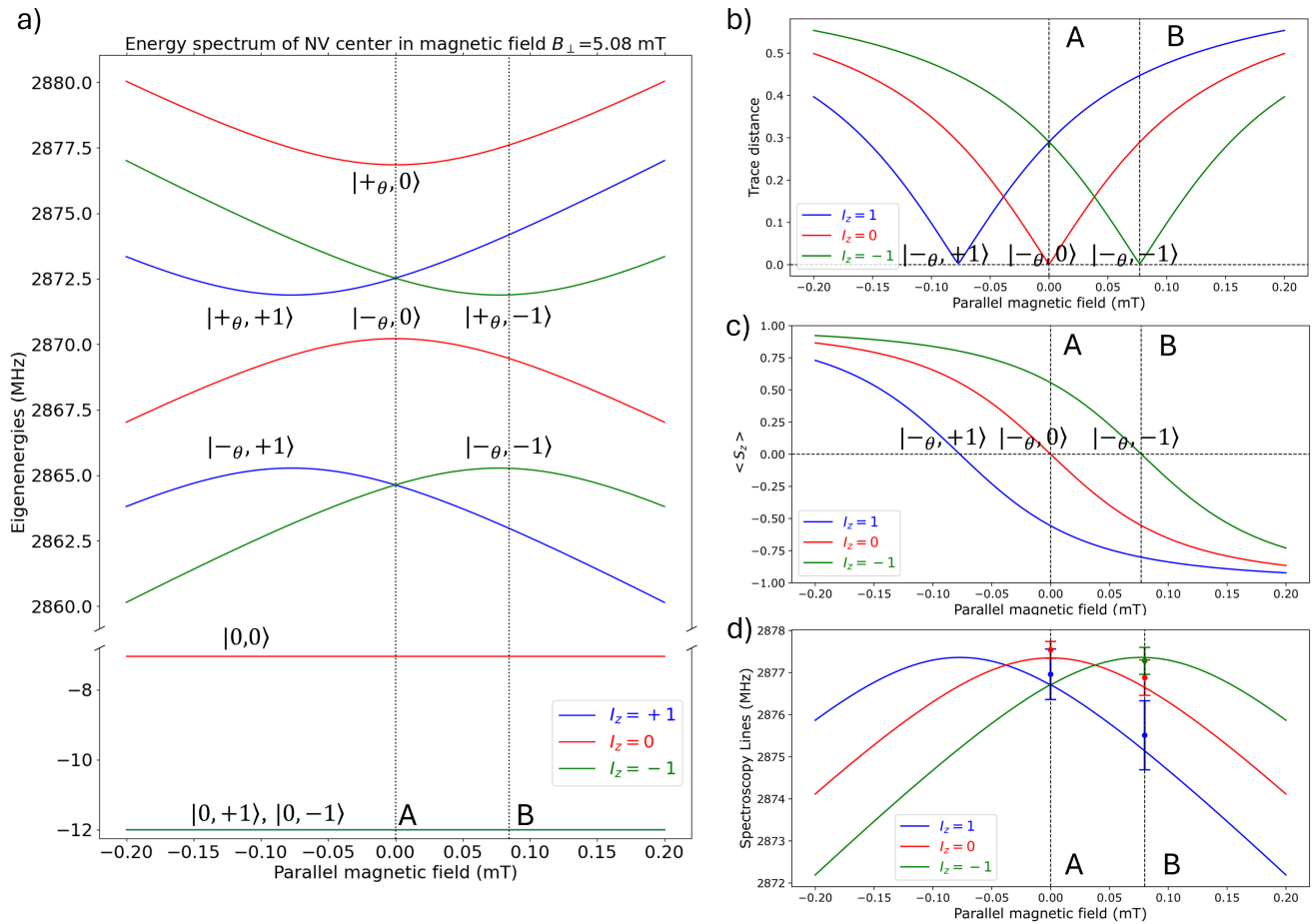


FIG. 1. (a) Eigenvalues of Hamiltonian in Eq. 1 as a function of axial magnetic field B_{\parallel} (B_{\perp} fixed). The curves are labeled according to the value of the spin eigenstates $|S_z, I_z\rangle$, where S_z and I_z are the axial components of electronic spin and nuclear spin respectively. In particular, the position of the dressed states $|+\theta, \cdot\rangle$ and $|-\theta, \cdot\rangle$ are depicted. (b) Trace distance between the density matrix derived from electronic dressed state $|-\theta\rangle$ and the density matrix derived from the eigenvectors of Eq. 1, as a function of the axial magnetic field B_{\parallel} . (c) Expectation values of S_z on the dressed states eigenvectors $|-\theta, \cdot\rangle$. (d) Resonance frequencies from $|0\rangle$ to the lower branch of excited states as a function of axial magnetic field B_{\parallel} . The energy differences are computed taking into account selection rules (the applied microwave couples with S_x and S_y , therefore $\Delta I_z = 0$, $\Delta S_z \pm 1$.) The circles represent the resonance frequencies derived from cw-ODMR spectra, see Figs.2a), 3a). The uncertainties on experimental data are the linewidths of the respective ODMR resonances.

a varying axial magnetic field B_{\parallel} . This orthogonal field has the form $\vec{B}_{\perp} = B_x \hat{x} + B_y \hat{y}$, with $B_x = 3.83$ mT, $B_y = 3.33$ mT. Additionally, an orthogonal total electric field $\vec{\Pi}_{\perp} = \Pi_x \hat{x} + \Pi_y \hat{y}$ is considered, with $\Pi_x = -124000$ V cm $^{-1}$ and $\Pi_y = -94000$ V cm $^{-1}$ (the values reported are obtained to match the experimental data, see Supplemental Material).

In the following, the effect of each term in Eq. 1 is analyzed to clarify the nature of the eigenstates, first by describing the effects of electronic interaction terms, and successively by including the nuclear interaction terms also.

1. Electronic Interaction terms

We start by considering the case where the nuclear spin interaction terms are neglected. This choice allows to limit the analysis to electron-related terms of the Hamiltonian only, as in ref. [13]. Here, the unperturbed Hamiltonian depends on the ground state crystal field splitting D_{gs} while the contributions from the orthogonal total electrical field $\vec{\Pi}_{\perp}$ and the orthogonal field \vec{B}_{\perp} are considered as perturbations, developing the perturbative solution up to the second order in eigenenergies. In the present analysis, instead the exact eigenstates are computed by diagonalization of the partial Hamiltonian containing only the electronic spin terms (zero-field, magnetic field, electric field) then, the newly obtained eigenstates and eigenenergies are expressed as a truncated

power series of the parameter $\zeta = \frac{g\epsilon\mu_B B_\perp}{D_{gs}}$ (for detailed calculations see Supplementary Materials).

The effect of D_{gs} is to create a large gap between the eigenenergy $E_{|S_z=0\rangle}$, relative to the eigenstate $|S_z=0\rangle$, and the eigenenergies $E_{|-\rangle} = E_{|+\rangle}$ relative to the two degenerate states $|-\rangle$ and $|+\rangle$. The combined contribution of the total orthogonal electric field $\vec{\Pi}_\perp$ (the effect of parallel strain Π_\parallel is negligible because $d_\parallel \ll d_\perp$) and weak orthogonal field \vec{B}_\perp can be summarized in four effects:

- Rotating the original dressed states $|0\rangle, |-\rangle, |+\rangle$ of an angle θ along the z -axis, giving the eigenstates $|0\rangle_\theta, |-\rangle_\theta, |+\rangle_\theta$. With

$$\theta = \frac{1}{2} \arg(e^{2i\phi_{B_\perp}} - 2R \cdot e^{-i\phi_\Pi}) \quad (2)$$

- Creating an energy gap between $|-\rangle_\theta$ and $|+\rangle_\theta$, where:

$$E_{gap} = 2 \left[\left(\frac{\mathcal{B}_\perp^2}{2D_{gs}} \right)^2 + \mathcal{E}^2 - \mathcal{E} \frac{\mathcal{B}_\perp^2}{D_{gs}} \cos(2\phi_{B_\perp} + \phi_\Pi) \right]^{\frac{1}{2}} \quad (3)$$

- Creating a small mixing, proportional to $\frac{\mathcal{B}}{D_{gs}}$, between $|+\rangle_\theta, |-\rangle_\theta$ and $|0\rangle$
- Decreasing the energy of the $|0\rangle$ state to $E_0 = -\frac{\mathcal{B}_\perp^2}{D_{gs}} < 0$

Where the following quantities are introduced:

$$\mathcal{B}_\perp = g\mu_B B_\perp, \quad \mathcal{E} = d_\perp \Pi_\perp, \quad R = \frac{\mathcal{E} D_{gs}}{\mathcal{B}_\perp^2}, \quad (4)$$

and

$$\phi_\Pi = \arctan\left(\frac{\Pi_y}{\Pi_x}\right), \quad \phi_{B_\perp} = \arctan\left(\frac{B_y}{B_x}\right) \quad (5)$$

The explicit expression of the rotated eigenstates are (for the detailed theoretical model, see the Supplementary Materials):

$$\begin{aligned} |0\rangle_\theta &= |0\rangle \\ |-\rangle_\theta &= \frac{1}{\sqrt{2}} (e^{-i\theta} |S_z = +1\rangle - e^{i\theta} |S_z = -1\rangle) \\ |+\rangle_\theta &= \frac{1}{\sqrt{2}} (e^{-i\theta} |S_z = +1\rangle + e^{i\theta} |S_z = -1\rangle) \end{aligned} \quad (6)$$

It is significant to study the dependency between θ and R , which are the rotation angle of dressed states

and the relative magnitude of Π_\perp and B_\perp respectively, since the latter is defining how dressed states are aligned with respect to bias electric and magnetic fields. First we consider the two limit cases for R : on the one hand, when the contribution of the orthogonal magnetic field B_\perp is predominant ($R \sim 0$) the eigenstates are rotated by ϕ_{B_\perp} , i.e. are aligned along the direction of B_\perp . On the other hand, when the contribution from the total orthogonal electric field Π is predominant ($R \gg 1$) the original eigenstates $|0\rangle, |-\rangle, |+\rangle$ are rotated by $\frac{\pi}{2} - \phi_\Pi/2$. For intermediate values of R , the competition between the orthogonal magnetic field B_\perp and the orthogonal total electric field Π results in a intermediate rotation between ϕ_{B_\perp} and $\frac{\pi}{2} - \phi_\Pi/2$, determined by the relative magnitude of B_\perp and Π_\perp . The general expression of θ shown in Eq.2 represents a first original result of this paper.

The eigenvectors in Eq.s 6 are still dressed states, i.e. a balanced superposition of strong-axial field states, thus being sensitive to the field \vec{B} only at second order since:

$$\begin{aligned} \theta \langle S_z = 0 | S_i | S_z = 0 \rangle_\theta &= \theta \langle - | S_i | - \rangle_\theta = \theta \langle + | S_i | + \rangle_\theta = 0 \\ \text{for } i &= x, y, z. \end{aligned} \quad (7)$$

By introducing a small axial magnetic field ($\mathcal{B}_\parallel^2 < E_{gap}/2$) and neglecting the minor mixing of $|+\rangle_\theta, |-\rangle_\theta$ with $|0\rangle$, the calculated eigenvectors become:

$$\begin{aligned} |-\rangle_{\theta, \mathcal{B}_\parallel} &= \sin\left(\frac{\gamma}{2}\right) |S_z = +1\rangle_\theta - \cos\left(\frac{\gamma}{2}\right) |S_z = -1\rangle_\theta \\ |+\rangle_{\theta, \mathcal{B}_\parallel} &= \cos\left(\frac{\gamma}{2}\right) |S_z = +1\rangle_\theta + \sin\left(\frac{\gamma}{2}\right) |S_z = -1\rangle_\theta \end{aligned} \quad (8)$$

while the corresponding eigenenergies are:

$$\begin{aligned} E_{0'}^{(2)} &= -\frac{\mathcal{B}_\perp^2}{2D_{gs}} \\ E_{-, \theta, \mathcal{B}_\parallel}^{(2)} &= D_{gs} + \frac{\mathcal{B}_\perp^2}{2D_{gs}} - \sqrt{(E_{gap}/2)^2 + \mathcal{B}_\parallel^2} \\ E_{+, \theta, \mathcal{B}_\parallel}^{(2)} &= D_{gs} + \frac{\mathcal{B}_\perp^2}{2D_{gs}} + \sqrt{(E_{gap}/2)^2 + \mathcal{B}_\parallel^2} \end{aligned} \quad (9)$$

with $\mathcal{B}_\parallel = g\mu_B B_\parallel$ and $\tan \gamma = \frac{E_{gap}}{2\mathcal{B}_\parallel}$ (see Supplemental Materials for a derivation of these equations).

For $\mathcal{B}_\parallel = 0$, one has $\frac{\gamma}{2} = \frac{\pi}{4}$ therefore the eigenstates are balanced superpositions of high field states. As \mathcal{B}_\parallel increases, $\frac{\gamma}{2}$ decreases, therefore the states become partially-dressed states and acquire a non-zero value of $\langle S_z \rangle$. For larger axial magnetic fields ($\mathcal{B}_\parallel^2 \gg (E_{gap}/2)^2$) the eigenenergies become linear in B_\parallel resulting in strong-axial field states.

Fig. 1(b) shows the trace distances between state $|-\rangle_\theta$ and the numerically evaluated eigenstates of the Hamiltonian in Eq. 1. The data regarding nuclear spin $I_z = 0$ (red curve) indicate that the two states are at zero distance for $B_\parallel = 0$ but, as B_\parallel increases, the distance be-

tween the states also increases. Additionally, with increasing B_{\parallel} the eigenstates acquire a non-zero value of $\langle S_z \rangle$ (Fig. 1(c)), as predicted by Eq.s 8.

2. Complete Hamiltonian

The interaction between NV electronic spin and ^{14}N nuclear spin \vec{I} is composed of two terms, quadrupolar and hyperfine interactions. The effect of the quadrupolar term is to turn I_z into a good quantum number and to increase the energy of states with $I_z = \pm 1$. The effect of the hyperfine term is noteworthy: It shifts the position of the dressed state from $B_{\parallel}^{\text{dressed}} = 0$ to $B_{\parallel}^{\text{dressed}} = \mp \frac{A_{\parallel}}{g\mu_B}$ for $I_z = \pm 1$. This phenomenon enables the simultaneous presence of dressed and partially dressed for the same applied field B_{\parallel} .

The analysis of the Complete Hamiltonian eigenenergies will focus on two values of B_{\parallel} :

- $B_{\parallel} = 0$ (point A in Fig. 1(d)). In this point, the eigenstates with $I_z = 0$ are dressed states, the eigenstates with $I_z = \pm 1$ are degenerate partially-dressed states, with opposite values of $\langle S_z \rangle$ [43]
- $B_{\parallel} = \frac{A_{\parallel}}{g\mu_B}$ (point B in Fig. 1(d)). In this point, the eigenstate with $I_z = -1$ is completely dressed, and the two other eigenstates are partially dressed.

As will be discuss later, working in point A is promising for quantum computation applications and working in point B is promising for quantum sensing applications.

III. EXPERIMENTAL RESULTS AND DISCUSSION

Our experimental investigation was performed onto an ensemble of $N \sim 6 \cdot 10^4$ independent NV centers distributed in a volume $V \sim 1 \cdot 10^{-17} \text{m}^3$, see Supplemental Material. Each NV is subjected to inhomogeneous magnetic and total effective electric fields, described by the distributions $P(B)$ and $P(\Pi)$. By reasonably neglecting the interaction between NV centers, the experimental results can be interpreted by solving Eq.1 for each value of B and Π . The eigenstate of the ensemble is the tensor product of the single NV density matrices, with each density matrix being weighted according to $P(B)$ and $P(\Pi)$. The eigenenergies of the ensemble are the weighted sum of a single NV density matrix according to $P(B)$ and $P(\Pi)$. The resonant frequency ν_{res} , which is computed from the differences in the eigenenergies, also follows a distribution $P(\nu_{res})$. In the following, two sets of results are presented: the first related to CW microwave excitation, the second to pulsed measurements.

1. Cw excitation

In a cw-ODMR measurement (see Fig.2(a) and 3(a)), an oscillating magnetic field with frequency ν_{MW} and a 532 nm laser are applied simultaneously (see Supplemental Materials for details on the experimental setup). The laser excitation has two effects: (i) inducing a red photoluminescence (PL), whose intensity depends on the spin state of the NV, with $|0\rangle$ being brighter than $|-\rangle_{\theta}$ and $|+\rangle_{\theta}$; and (ii) it polarizes the NV in spin state $|0\rangle$. To explain the technique, let's focus on states $|0\rangle$ and $|-\rangle_{\theta}$. If ν_{MW} is far from the resonant frequency $\nu_{res} = (E_{|0\rangle} - E_{|-\rangle_{\theta}}) / \hbar$, the oscillating magnetic field is not effective in driving transitions between $|0\rangle$ and $|-\rangle_{\theta}$, moreover, the green light polarizes the NV state to $|0\rangle$, resulting in brighter PL emission. Conversely, when $\nu_{MW} = \nu_{res} = (E_{|0\rangle} - E_{|-\rangle_{\theta}}) / \hbar$, the oscillating field is very effective in driving transitions between $|0\rangle$ and $|-\rangle_{\theta}$, therefore the dark state $|-\rangle_{\theta}$ is populated and the collected PL presents a minimum [44]. In Fig. 1 (point A), two resonances are observable for $B_{\parallel} = 0$, one related to a dressed state, $\nu_{A,dres}$, and the other, $\nu_{A,p-dres1}$, related to two degenerate partially-dressed states with opposite values of $\langle S_z \rangle$, as predicted numerically (see Fig. 1 (c) and (d)). The two transitions are clearly visible in the ODMR spectrum in Fig. 2(a). The resonance corresponding to $I_z = \pm 1$ presents a greater contrast due to the presence of the two degenerate populations. In point B, for $B_{\parallel} = \frac{A_{\parallel}}{g\mu_B}$, there are three resonant frequencies: one corresponding to a dressed state, $\nu_{B,dres}$, and two corresponding to partially dressed states with different non-zero values of $\langle S_z \rangle$, $\nu_{B,p-dres2}$ ($I_z = 0$) and $\nu_{B,p-dres3}$ ($I_z = +1$). The three resonances are clearly visible in the ODMR spectrum in Fig. 3 (a). It is important to underline that $\nu_{A,dres} = \nu_{B,dres}$ because in point B the axial field compensates the hyperfine term, while the contribution of the nuclear quadrupolar term is equivalent both for $|0, 1\rangle$ and $|-\theta, 1\rangle$, therefore it does not enter in the derivation of $\nu_{B,dres}$. The different states are excited by different polarizations of the oscillating field. It is interesting because in a NV ensemble where dressed, partially dress, and hgh fiuledl states are present, the different polarizations enable to be selective on states excitation, eg. Rabi and FID measurements Dressed states are excited by an oscillating magnetic field which is linearly polarized in the x-y plane and aligned along the direction defined by the angle θ in Eq 2. High-field states are excited by an oscillating magnetic field which is circularly polarized in the x-y plane, and that can be viewed as the balanced sum of two oscillating fields linearly polarized along orthogonal directions. Partially dressed states are polarized by an oscillating magnetic field elliptically polarized in the x-y plane, which is as the unbalanced sum of two oscillating fields, one polarized along θ and the other along a direction orthogonal to θ . This topic is extensively discussed

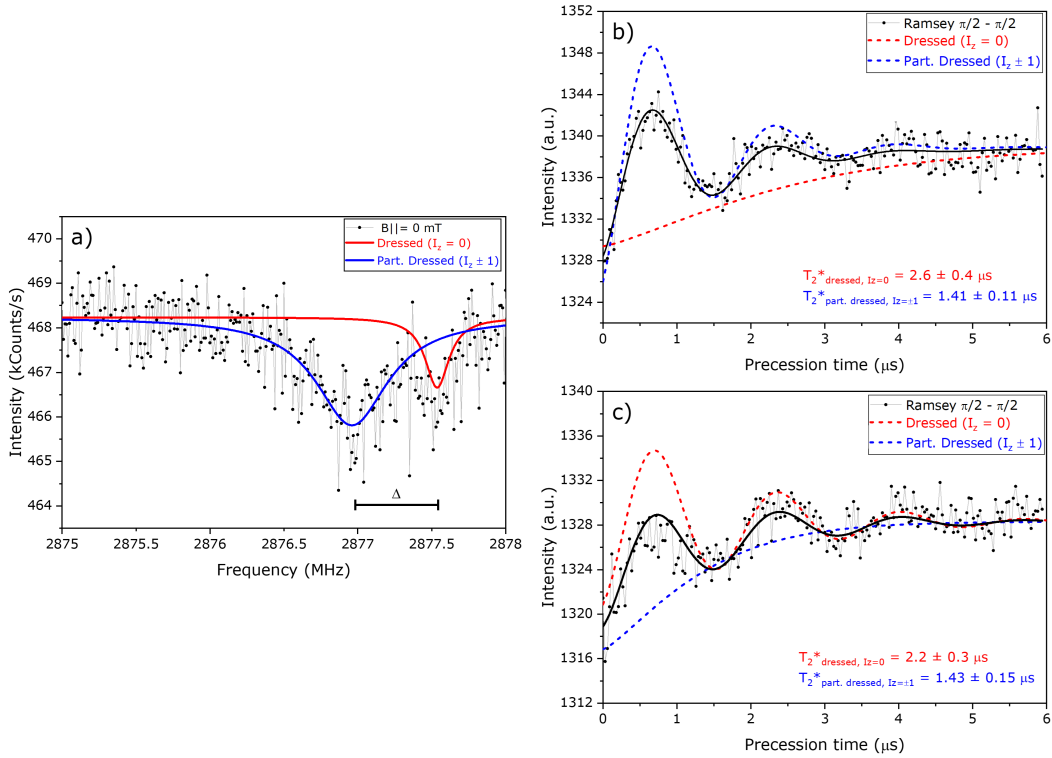


FIG. 2. Experimental results for $B_{\parallel} = 0$, corresponding to point A in Fig. (1): (a) Optically Detected Magnetic Resonance spectra. Two resonances are present. The one at smaller frequency $\nu_{A,p-dres1}$ is related to two degenerate partially-dressed states, corresponding to the nuclear spin states $I_z = \pm 1$. The blue solid line fits this resonance following a Lorentzian distribution. The one at the larger frequency $\nu_{A,dres}$ is related to the dressed state and corresponds to the nuclear spin state $I_z = 0$. The red solid line fits this resonance following a Lorentzian distribution. The difference $\Delta = \nu_{A,dres} - \nu_{A,p-dres1}$ between the two resonance frequencies is indicated. (b) Free Induction Decay relaxation for a microwave of frequency $\nu_{MW} = \nu_{A,dres}$ on resonance with the dressed state $I_z = 0$. The decay is fitted as the contribution of a pure stretched exponential, red dashed curve, and an oscillating stretched exponential, blue dashed curve. The pure stretched exponential is related to the dressed state with $I_z = 0$. The explicit expression of the decay used in the fit is $f(y) = y_0 + Ae^{(-t/T_{2,dressed}^{*} I_z=0)^p}$. The oscillating stretched exponential is related to the partially dressed states with $I_z = \pm 1$. The explicit expression of the decay used in the fit is $f(y) = y_0 + Ae^{(-t/T_{2,part. dressed-1}^{*} I_z=\pm 1)^p} \cos(2\pi\Delta t + \phi)$. (c) Free Induction Decay relaxation for a microwave of frequency $\nu_{MW} = \nu_{A,p-dres1}$ on resonance with the degenerate partially dressed states $I_z = \pm 1$. The decay is fitted as the contribution of a pure stretched exponential, blue dashed curve, and an oscillating stretched exponential, red dashed curve. The pure stretched exponential is related to the partially-dressed states with $I_z = \pm 1$. The explicit expression of the decay used in the fit is $f(y) = y_0 + Ae^{(-t/T_{2,part. dressed-1}^{*} I_z=\pm 1)^p}$. The oscillating stretched exponential is related to the dressed state with $I_z = 0$. The explicit expression of the decay used in the fit is $f(y) = y_0 + Ae^{(-t/T_{2,dressed}^{*} I_z=0)^p} \cos(2\pi\Delta t + \phi)$. In all curves, the value of the stretched exponential is fixed to $p = 1.24$, derived from the fit of the decaying of strong axial field states.

in the Supplementary Materials. An oscillating magnetic field linearly polarized in the x-y plane along an angle different from θ is used. This oscillating magnetic field can be viewed as the sum of two linearly polarized fields, one polarized along θ and the other in a direction orthogonal to θ . In this way, we can excite both dressed and partially dressed states.

cw-ODMR spectra hint at the different behaviors of dressed and partially dressed states, notably, the former ones exhibit narrower transition linewidths with respect to the latter ones. This is because the dressed states are sensitive only at the second order to noise coming from: coupling with the spin baths and inhomogeneities in the external magnetic field B ; when these are the two main

sources of decoherence, dressed states are expected to show longer coherence times T_2^* (see Supplemental Materials). cw-ODMR measurements are not ideal for discriminating between dressed and partially dressed states due to the effect of power broadening: to clearly resolve peaks linked to the different states, it would be required to decrease the microwave (MW) power, however, this would also decrease the contrast and reduce the overall S/N ratio.

Hence, Free Induction Decay (FID) measurements are selected to characterize the different types of states as these are not affected by mw-power broadening and can give a direct evaluation of T_2^* .

2. Pulsed measurements

In general, FID measurements are composed of: an initialization optical pulse, two $\frac{\pi}{2}$ mw pulse separated by a free precession interval of duration τ and a final readout optical pulse (see Supplemental Material). The system is initialized in the state $|0\rangle$, the first $\frac{\pi}{2}$ pulse brings the state in a superposition of $|0\rangle$ and $|S_z \neq 0\rangle$. During the free evolution time, the two components of the superposition acquire a phase difference ϕ depending on the detuning $\Delta = \nu_{MW} - \nu_{res}$ between mw excitation frequency ν_{MW} and the resonant frequency ν_{res} . The second $\frac{\pi}{2}$ encodes ϕ in the population of the $|0\rangle$ state ($p_{|0\rangle}$) [45]. The final read-out optical pulse excites a PL proportional to $p_{|0\rangle}$. The output PL signal is measured with a single-photon detector in a confocal microscopy setup (see [46] and Supplemental Materials). The general form of $p_{|0\rangle}$ for a FID measurement where a single resonance is driven is:

$$p_{|0\rangle}(\tau) = \frac{1}{2} \left[1 - e^{-\left(\frac{\tau}{T_2^*}\right)^\beta} \cos(2\pi\Delta\tau) \right] \quad (10)$$

with $1 \leq \beta < 2$. The coherence time T_2^* defines the scale on which the system loses quantum coherence, and the population decays of a factor $\frac{1}{2}$, corresponding to a completely mixed state. For an ensemble of NVs, the decay is caused by different sources of decoherence: coupling with surrounding spins, temporal fluctuations and spatial gradients in the external fields B_i and Π_i [47, 48]. The value of β gives information on the relative weight of the different sources of decoherence: if $\beta \sim 1$ the main source of decoherence is coupling with surrounding spins, while an increase in β corresponds to a greater influence of temporal fluctuations and spatial gradients of the external fields [47–49]. If the microwave pulse $\frac{\pi}{2}$ has enough spectral width [50] to drive more than one resonance, the PL signal is the sum of multiple terms analogous to Eq.10 but with different $\Delta_i = \nu_{MW} - \nu_{res,i}$.

Our measurements (Fig2) were collected with $B_{\parallel} = 0$, corresponding to point A in Fig.s 1. The spectral width is sufficient to excite both resonances. First, we consider a FID measurement on resonance with the dressed state with $I_z = 0$, $\nu_{MW} = \nu_{A,dres}$, shown in Fig. 2 (b). The experimental curve is the sum of a pure stretched exponential and an oscillating stretched exponential. The pure stretched exponential is associated with a detuning $\Delta\nu = 0$, corresponding to the resonance of the dressed state. The oscillating exponential is associated with a detuning $\Delta = 532$ kHz, corresponding to the resonance of a partially-dressed state. The coherence time T_2^* of dressed states is 1.3 times longer than that of the partially dressed state, as listed in Table I. A similar improvement in T_2^* is observed when the FID measurement is performed on resonance with the degenerate partially-dressed states with $I_z = \pm 1$, $\nu_{MW} = \nu_{A,p-dres1}$, as shown in Fig. 2

(c). In this case, the pure exponential is related to the partially-dressed state and the oscillating exponential is related to the dressed state. Moreover, the values of T_2^* for dressed states are compatible among measurements performed on resonance with different transitions, this behavior can be observed also for the values of T_2^* for partially-dressed states. A quick observation of the experimental decays in Fig.s 2 confirms the previous finding: oscillations last longer when the detuned state is the dressed state. FID measurements were also conducted for another sub-ensemble with a different NV-axis orientation, as detailed in the Supplemental Materials, that exhibited a component along the z-axis $B_{\parallel} = 0.871$ mT. The FID data were recorded by tuning the mw frequency on resonance with the central hyperfine peak, thus only a single detuning ($\nu = 2.16$ MHz) is observed. As described in the previous section, strong axial field states couple with the spin bath and fluctuations of external magnetic fields, leading to shorter coherence times than dressed states. In this case, the axial field is much larger than the orthogonal field, therefore the eigenstates are pure strong-axial-field states, resulting in T_2^* that is more than two times shorter than the one obtained for dressed states, as shown in Table I.

Dressed states, partially-dressed states and strong-axial field states present different coherence times as they are affected differently by the various sources of decoherence. Dressed states are more sensitive to temporal fluctuation and inhomogeneities of total electric field $\vec{\Pi}$, because $\langle S_x^2 - S_y^2 \rangle \neq 0$, $\langle S_x S_y + S_y S_x \rangle \neq 0$ which are the coupling terms for Π_x and Π_y in the Hamiltonian presented in Eq.1, while $\langle S_z \rangle = 0$. Strong-axial field states are more sensitive to dipolar coupling with the surrounding spin bath, temporal fluctuation and spatial gradients of the axial magnetic field B_{\parallel} because $\langle S_z \rangle \neq 0$ while $\langle S_x^2 - S_y^2 \rangle$, $\langle S_x S_y + S_y S_x \rangle = 0$. On the other hand, for partially dressed state, $\langle S_z \rangle \neq 0$ and $\langle S_x^2 - S_y^2 \rangle$, $\langle S_x S_y + S_y S_x \rangle \neq 0$, therefore the different sources of decoherence compete. For more details on this topic, see [35] and Supplemental Material. The decrease in coherence time T_2^* observed when passing from dressed states to partially dressed states then to strong axial field states indicates that dipolar coupling with surrounding spin baths and temporal fluctuations and spatial inhomogeneities of the axial magnetic field are the major sources of decoherence in the sample being studied. This can be explained by the high concentration of ^{14}N spin centers that couple to NVs as a consequence of the large implantation fluence employed ($F = 1 \cdot 10^{14}$).

The stretched exponential parameter β should be different for dressed, partially dressed, and strong axial field states. The impact of dipolar coupling on surrounding spin baths tends to drive β towards 1, while gradients and temporal fluctuations of B_{\parallel} and $\vec{\Pi}$ tend to drive β towards 2. Dressed states are more influenced by inhomogeneities and temporal fluctuations of $\vec{\Pi}$, therefore a value of β close to 2 is expected. For strong axial field states, instead, a value of β close to 1 is expected due

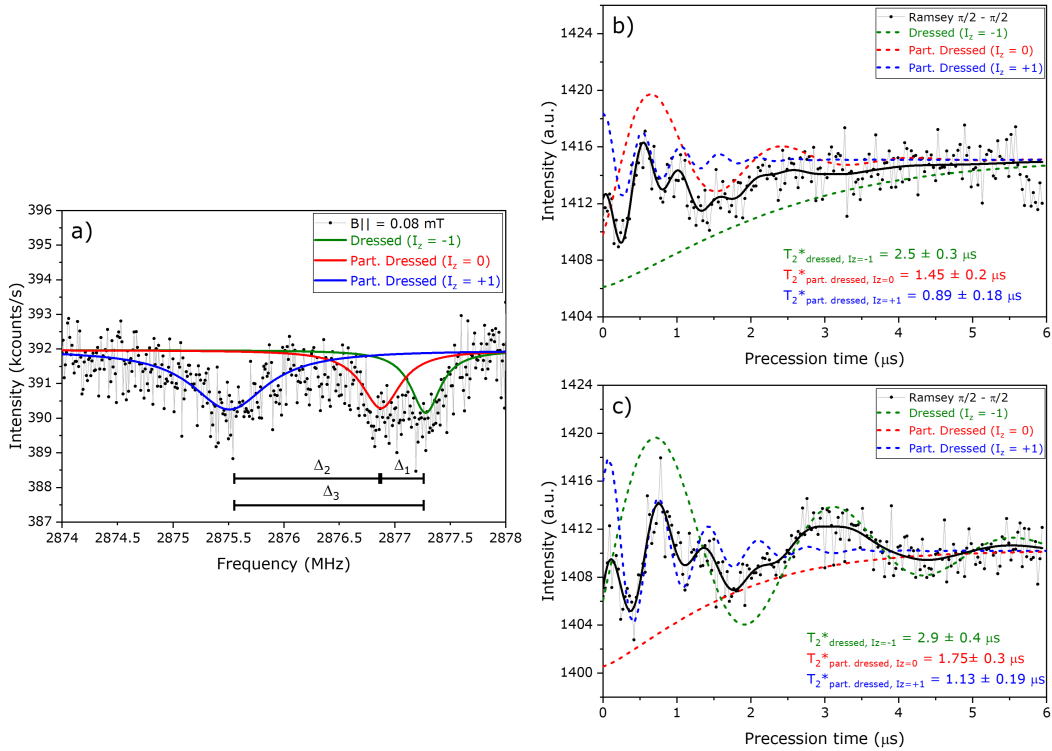


FIG. 3. Experimental results for $B_{\parallel} = 0.8$ mT, corresponding to point B in Fig. (1): (a) Optically Detected Magnetic Resonance spectra. Three resonances are present. The one at smaller frequency $\nu_{B,p-dres3}$ is related to a partially-dressed state, corresponding to the nuclear spin states $I_z = +1$. The blue solid line fits this resonance following a Lorentzian distribution. The one at intermediate frequency $\nu_{B,p-dres2}$ is related to another partially-dressed state, corresponding to the nuclear spin states $I_z = 0$. The red solid line fits this resonance following a Lorentzian distribution. The one at the larger frequency $\nu_{B,dres}$ is related to the dressed state and corresponds to the nuclear spin state $I_z = -1$. The green solid line fits this resonance following a Lorentzian distribution. The three frequency differences $\Delta_1 = \nu_{B,dres} - \nu_{B,p-dres2}$, $\Delta_2 = \nu_{B,p-dres2} - \nu_{B,p-dres3}$, $\Delta_3 = \nu_{B,dres} - \nu_{B,p-dres3}$ are indicated. (b) Free Induction Decay relaxation for a microwave of frequency $\nu_{MW} = \nu_{B,dres}$ on resonance with the dressed state $I_z = -1$. The decay is fitted as the contribution of a pure stretched exponential, green dashed curve, and two oscillating stretched exponentials, red dashed curve and blue dashed curve. The pure stretched exponential is related to the dressed state with $I_z = -1$. The explicit expression of the decay used in the fit is $f(y) = y_0 + Ae^{(-t/T_{2,dressed}^{I_z=-1})^p}$. The slower oscillating exponential is related to the partially dressed state with $I_z = 0$. The explicit expression of the decay used in the fit is $f(y) = y_0 + Ae^{(-t/T_{2,part. dressed-2}^{I_z=0})^p} \cos(2\pi\Delta_1 t + \phi)$. The faster oscillating exponential is related to the partially dressed state with $I_z = +1$. The explicit expression of the decay used in the fit is $f(y) = y_0 + Ae^{(-t/T_{2,part. dressed-3}^{I_z=0})^p} \cos(2\pi\Delta_3 t + \phi)$. (c) Free Induction Decay relaxation for a microwave of frequency $\nu_{MW} = \nu_{B,p-dres2}$ on resonance with the dressed state $I_z = 0$. The decay is fitted as the contribution of a pure stretched exponential, red dashed curve, and two oscillating stretched exponentials, green dashed curve and blue dashed curve. The pure stretched exponential is related to the partially dressed state with $I_z = 0$. The explicit expression of the decay used in the fit is $f(y) = y_0 + Ae^{(-t/T_{2,part. dressed-2}^{I_z=0})^p}$. The slower oscillating exponential is related to the dressed state with $I_z = -1$. The explicit expression of the decay used in the fit is $f(y) = y_0 + Ae^{(-t/T_{2,dressed}^{I_z=-1})^p} \cos(2\pi\Delta_1 t + \phi)$. The faster oscillating exponential is related to the partially dressed state with $I_z = +1$. The explicit expression of the decay used in the fit is $f(y) = y_0 + Ae^{(-t/T_{2,part. dressed-3}^{I_z=0})^p} \cos(2\pi\Delta_2 t + \phi)$. The value of the stretched exponential is fixed to $p = 1.24$, derived from the fit of the decaying of strong axial field states

to the effect of the spin bath. In general, the value of β is set by the competition between these decoherence sources and the values of field gradients. For simplicity, the value $\beta = 1.28$ obtained from the single decay of strong-axial field states is used as a fixed parameter for both dressed and partially dressed decays, taking into account that a considerable uncertainty is associated with the estimation of β (see Supplemental Materials).

The main result of this work is described by the ex-

perimental data shown in Fig.2, which clearly indicate the ability to coherently drive two resonance states associated with different values of the nuclear spin I_z , while extending the coherence time T_2^* with respect to the typically used strong-axial field state. This opens up the potential for leveraging the weak orthogonal field regime to achieve high fidelity $C_e\text{NOT}_n$ gates, which are essential for quantum computation and have also been recently employed to enhance the sensitivity of magnetic mea-

	T_2^* dressed	T_2^* part-dressed-1	T_2^* part-dressed-2	T_2^* part-dressed-3	T_2^* Strong-axial Field
$B_{\parallel} = 0(\text{A}), \nu_{MW} = \nu_{A,dres}$	2.6 ± 0.4	1.41 ± 0.11	-	-	-
$B_{\parallel} = 0(\text{A}), \nu_{MW} = \nu_{A,p-dres1}$	2.2 ± 0.3	1.43 ± 0.15	-	-	-
$B_{\parallel} = \frac{A_{\parallel}}{g\mu_B}(\text{B}), \nu_{MW} = \nu_{B,dres}$	2.3 ± 0.3	-	1.43 ± 0.15	0.89 ± 0.18	-
$B_{\parallel} = \frac{A_{\parallel}}{g\mu_B}(\text{B}), \nu_{MW} = \nu_{B,p-dres2}$	2.9 ± 0.4	-	1.75 ± 0.15	1.13 ± 0.19	-
Strong-axial Field	-	-	-	-	$0.88. \pm 0.17$

TABLE I. Values of coherence time T_2^* , derived from the fit of the Free Induction Decays for different experimental conditions. Each row corresponds to a value of axial field B_{\parallel} and of microwave frequency ν_{MW} .

surements [51]. A basic $C_e\text{NOT}_n$ gate can be realized by employing the FID sequence and adjusting the free evolution time to $\tau = \frac{\pi}{\Delta}$, which corresponds to the half period of the decaying oscillations.

It is important to underline that dressed states are sensitive to the magnetic field only at the second order. Instead, the partially-dressed states are sensitive to the magnetic field at the first order, being characterized by a non-zero expectation value of the axial spin $\langle S_z \rangle \neq 0$. This paves the way to applications in magnetic field sensing. For this kind of application, working in point A in Fig. 1 is not ideal. In point A, The degenerate partially-dressed states correspond to two opposite values of $\langle S_z \rangle$, and a magnetic field B_{\parallel}^{sense} will cause two opposite detunings [52]. The effect of these detunings will tend to cancel each other on a typical magnetic field measurement. For these reasons, we apply a small bias magnetic field $B_{\parallel} = \frac{A_{\parallel}}{g\mu_B} = 0.08$ mT, corresponding to point B of Fig. 1, where there are three resonances, one ν_1 , belonging to a dressed state, and two ν_2 and ν_3 belonging to two partially-dressed states with two different values of $\langle S_z \rangle$.

The results of FID measurement performed under this regime are shown in Figs 3(b)-(c). Fig.3(b) shows a measurement taken on resonance with the $I_z = -1$ state ($\nu_{mw} = \nu_{B,dres}$), where a combination of three resonance contributions, as in Eq.10, properly describes the experimental data. One component is a very slow oscillating exponential, associated with the on-resonance dressed state with $I_z = -1$. This slow oscillation is due to non-optimal experimental condition. Then, there are two faster-oscillating exponentials corresponding to detunings $\Delta_1 = \nu_{B,dres} - \nu_{B,p-dres2}$ and $\Delta_3 = \nu_{B,dres} - \nu_{B,p-dres3}$, which belong to two partially dressed states. The different components exhibit different T_2^* values. Similarly to point A, the dressed states exhibit a longer T_2^* than partially dressed states. Moreover, T_2^* decreases moving from partially-dressed state 2 to partially-dressed state 3 because there is an associated increase in $\langle S_z \rangle$. A similar behavior in T_2^* is observed when FID measurements are performed on resonance with partially-dressed state having $I_z = 0$ ($\nu_{mw} = \nu_{B,p-dres2}$), 3(c). In this case there is one very slow oscillating exponential associated with the on resonance partially-dressed state $I_z = 0$. Again, this slow oscillation is due to non-optimal experimental conditions. Then there are two faster oscillating exponential corresponding to the detunings $\Delta_1 = \nu_{B,p-dres2} - \nu_{B,dres}$

and $\Delta_2 = \nu_{B,p-dres2} - \nu_{B,p-dres3}$. Under these experimental conditions as well, the value of T_2^* depends on the degree to which a state is dressed and not on the value of the driving microwave frequency ν_{MW} .

The claim of this work is that a sensing regime working in point B in Figs 1 represents an interesting alternative to current methods[17–19, 21] to decouple the effects of different external variables (e.g. magnetic, electric field, strain, temperature, etc) on the ODMR resonance. Here it is shown the ability to selectively drive the magnetic-independent resonance $\nu_{B,dres}$ and the magnetic dependent resonance $\nu_{B,p-dres2}$ using quantum optimal control techniques [53]. For instance, to detect a variation of axial magnetic field ΔB_{\parallel} in presence of a temperature variation ΔT , it is possible to measure the detuning Δ_1 , which is not sensitive to ΔB_{\parallel} and use it as a reference to subtract detuning Δ_2 that depends on ΔB_{\parallel} . The two resonances can be driven selectively by using a single microwave frequency modulated pulse with a bandwidth of 5 MHz, as they are separated only by $\nu_{B,dres} - \nu_{B,p-dres2} = 532$ KHz. Another possibility is to create a superposition of nuclear states, $|S_z = 0\rangle \otimes \frac{1}{2}(|I_z = +1\rangle + |I_z = 0\rangle)$, and then apply a sequence of rectangular pulses that excite both resonances, similar to the ones used for quantum beats magnetometry and thermal echo. Generally with these techniques, the states being simultaneously affected are the typical strong-axial field states $|S_z = +1\rangle$ and $|S_z = -1\rangle$, while in this case the dressed and partially dressed states would be used. The primary advantage of our proposal is that the dressed and partially dressed states are closer in frequency at working point B compared to the $|S_z = +1\rangle$ and $|S_z = -1\rangle$ states in strong axial field configuration. This allows for the use of lower power pulses, providing an advantage, for instance, in sensing biological systems.

IV. CONCLUSIONS

Free Induction Decay (FID) measurements have been conducted in the presence of a weak orthogonal field and a total electric field for an ensemble of Nitrogen-Vacancy centers. First, the competition between the weak orthogonal field and the total electric field was considered, showing that the resulting eigenstates are dressed states, balanced superposition of strong axial field states, rotated in the orthogonal plane. The explicit formula for

the rotation angle was obtained from the expression of the exact eigenstates (up to now in literature only calculations in the perturbative approach were available). Then, the role of axial magnetic fields in creating unbalanced superposition of strong axial field states, which we call partially-dressed states, was described. Two working points were studied experimentally: one with a null axial magnetic field applied, and a second with an axial magnetic field matching the hyperfine field caused by the ^{14}N nucleus. In both working points, we observed the presence of dressed states and partially dressed states in the FID measurements. Dressed and partially dressed states can be distinguished by different coherence times T_2^* which shows a decrease when transitioning from dressed to partially dressed states. Compared to the widely studied strong-axial field states, the coherence time T_2^* is enhanced in dressed states and partially dressed states. The possibility to simultaneously drive dressed and partially dressed states using a single microwave opens up interesting applications in quantum computation and quantum sensing. More specifically, we refer to the work presented in ref [54]. This work uses a

repetitive readout protocol on NV ensemble. We can use the findings of the present paper for the selective magnetic field sensing part and the $C_e\text{NOT}_n$ to write the state on the N nucleus.

ACKNOWLEDGMENTS

E.B. thanks A. Rigamonti for introducing him to Magnetic Resonance. The work has received funding from the European Partnership on Metrology 23NRM04 NoQTeS project, co-financed from the European Union's Horizon Europe Research and Innovation Programme and by the Participating States; Projects Qutenoise and Trapezio of San Paolo Foundation; Project INFN QUISS. The authors wish to acknowledge the National Collaborative Research Infrastructure Strategy (NCRIS) funding provided by the Australian Government for this research. The authors wish also to thank F. Saccomandi for collaborating in the development of the magnetic field control system.

-
- [1] C. L. Degen, F. Reinhard, and P. Cappellaro, Quantum sensing, *Reviews of Modern Physics* **89**, 035002 (2017).
- [2] G. Petrini, E. Moreva, E. Bernardi, P. Traina, G. Tomagra, V. Carabelli, I. P. Degiovanni, and M. Genovese, Is a quantum biosensing revolution approaching? perspectives in nv-assisted current and thermal biosensing in living cells, *Advanced Quantum Technologies* **3**, 2000066 (2020).
- [3] E. Oh, M. D. Gregoire, A. T. Black, K. J. Hughes, P. D. Kunz, M. Larsen, J. Lautier-Gaud, J. Lee, P. D. D. Schwindt, S. L. Mouradian, F. A. Narducci, and C. A. Sackett, A perspective on quantum sensors from basic research to commercial applications (2024), arXiv:2407.00689 [quant-ph].
- [4] M. Genovese, Experimental quantum enhanced optical interferometry, *AVS Quantum Science* **3**, 044702 (2021), <https://pubs.aip.org/avs/aqs/article-pdf/doi/10.1116/5.0062114/14086685/044702.1.online.pdf>.
- [5] A. Karsa, A. Fletcher, G. Spedalieri, and S. Pirandola, Quantum illumination and quantum radar: a brief overview, *Reports on Progress in Physics* **87**, 094001 (2024).
- [6] R. Gallego Torromé and S. Barzanjeh, Advances in quantum radar and quantum lidar, *Progress in Quantum Electronics* **93**, 100497 (2024).
- [7] G. Brida, M. Genovese, A. Meda, and I. R. Berchera, Experimental quantum imaging exploiting multimode spatial correlation of twin beams, *Phys. Rev. A* **83**, 033811 (2011).
- [8] Y. Israel, Supersensitive polarization microscopy using noon states of light, *Physical Review Letters* **112**, 103604 (2024).
- [9] J. Aasi, J. Abadie, B. Abbott, *et al.*, Enhanced sensitivity of the ligo gravitational wave detector by using squeezed states of light, *Nature Photonics* **7**, 613 (2013).
- [10] B. Stray, A. Lamb, A. Kaushik, J. Vovrosh, A. Rodgers, F. Winch, Jand Hayati, D. Boddice, A. Stabrawa, A. Niggebaum, M. Langlois, Y.-H. Lien, S. Lellouch, S. Roshanmanesh, K. Ridley, G. de Villiers, G. Brown, T. Cross, G. Tuckwell, A. Faramarzi, N. Metje, K. Bongs, and M. Holynski, Quantum sensing for gravity cartography, *Nature* **602**, 590 (2022).
- [11] S. Magaletti, L. Mayer, J.-F. Roch, and T. Debuisschert, A quantum radio frequency signal analyzer based on nitrogen vacancy centers in diamond, *Communications Engineering* **1**, 19 (2022).
- [12] S. Hernández-Gómez, T. Isogawa, A. Belenchia, A. Levy, N. Fabbri, S. Gherardini, and P. Cappellaro, Interferometry of quantum correlation functions to access quasiprobability distribution of work, *npj Quantum Information* **10** (2024).
- [13] M. Doherty, F. Dolde, H. Fedder, F. Jelezko, J. Wrachtrup, N. Manson, and L. Hollenberg, Theory of the ground-state spin of the nv-center in diamond, *Physical Review B* **85**, 205203 (2012).
- [14] M. W. Doherty, N. B. Manson, P. Delaney, F. Jelezko, J. Wrachtrup, and L. C. Hollenberg, The nitrogen-vacancy colour centre in diamond, *Physics Reports* **528**, 1 (2013).
- [15] L. Rondin, J.-P. Tetienne, T. Hingant, J.-F. Roch, P. Maletinsky, and V. Jacques, Magnetometry with nitrogen-vacancy defects in diamond, *Reports on progress in physics* **77**, 056503 (2014).
- [16] B. Ofori-Okai, S. Pezzagna, K. Chang, M. Loretz, R. Schirhagl, Y. Tao, B. Moores, K. Groot-Berning, J. Meijer, and C. Degen, Spin properties of very shallow nitrogen vacancy defects in diamond, *Physical Review B?Condensed Matter and Materials Physics* **86**, 081406 (2012).

- [17] D. M. Toyli, C. F. de Las Casas, D. J. Christle, V. V. Dobrovitski, and D. D. Awschalom, Fluorescence thermometry enhanced by the quantum coherence of single spins in diamond, *Proceedings of the National Academy of Sciences* **110**, 8417 (2013).
- [18] P. Neumann, I. Jakobi, F. Dolde, C. Burk, R. Reuter, G. Waldherr, J. Honert, T. Wolf, A. Brunner, J. H. Shim, *et al.*, High-precision nanoscale temperature sensing using single defects in diamond, *Nano letters* **13**, 2738 (2013).
- [19] K. Fang, V. M. Acosta, C. Santori, Z. Huang, K. M. Itoh, H. Watanabe, S. Shikata, and R. G. Beausoleil, High-sensitivity magnetometry based on quantum beats in diamond nitrogen-vacancy centers, *Physical review letters* **110**, 130802 (2013).
- [20] L. M. Pham, N. Bar-Gill, C. Belthangady, D. Le Sage, P. Cappellaro, M. D. Lukin, A. Yacoby, and R. L. Walsworth, Enhanced solid-state multispin metrology using dynamical decoupling, *Phys. Rev. B* **86**, 045214 (2012).
- [21] P. Kehayias, M. Mrózek, V. M. Acosta, A. Jarmola, D. Rudnicki, R. Folman, W. Gawlik, and D. Budker, Microwave saturation spectroscopy of nitrogen-vacancy ensembles in diamond, *Physical Review B* **89**, 245202 (2014).
- [22] J. F. Barry, J. M. Schloss, E. Bauch, M. J. Turner, C. A. Hart, L. M. Pham, and R. L. Walsworth, Sensitivity optimization for nv-diamond magnetometry, *Reviews of Modern Physics* **92**, 015004 (2020).
- [23] G. Kucsko, P. C. Maurer, N. Y. Yao, M. Kubo, H. J. Noh, P. K. Lo, H. Park, and M. D. Lukin, Nanometre-scale thermometry in a living cell, *Nature* **500**, 54 (2013).
- [24] G. Petrini, G. Tomagra, E. Bernardi, E. Moreva, P. Traina, A. Marcantoni, F. Picollo, K. Kvaková, P. Cíglér, I. P. Degiovanni, *et al.*, Nanodiamond-quantum sensors reveal temperature variation associated to hippocampal neurons firing, *Advanced Science* **9**, 2202014 (2022).
- [25] M. Fujiwara, S. Sun, A. Dohms, Y. Nishimura, K. Suto, Y. Takezawa, K. Oshimi, L. Zhao, N. Sadzak, Y. Umehara, *et al.*, Real-time nanodiamond thermometry probing in vivo thermogenic responses, *Science advances* **6**, eaba9636 (2020).
- [26] I. Lovchinsky, A. Sushkov, E. Urbach, N. P. de Leon, S. Choi, K. De Greve, R. Evans, R. Gertner, E. Bersin, C. Müller, *et al.*, Nuclear magnetic resonance detection and spectroscopy of single proteins using quantum logic, *Science* **351**, 836 (2016).
- [27] D. R. Glenn, D. B. Bucher, J. Lee, M. D. Lukin, H. Park, and R. L. Walsworth, High-resolution magnetic resonance spectroscopy using a solid-state spin sensor, *Nature* **555**, 351 (2018).
- [28] L. Thiel, D. Rohner, M. Ganzhorn, P. Appel, E. Neu, B. Müller, R. Kleiner, D. Koelle, and P. Maletinsky, Quantitative nanoscale vortex imaging using a cryogenic quantum magnetometer, *Nature nanotechnology* **11**, 677 (2016).
- [29] M. Abobeih, Y. Wang, J. Randall, S. Loenen, C. Bradley, M. Markham, D. Twitchen, B. Terhal, and T. Taminiau, Fault-tolerant operation of a logical qubit in a diamond quantum processor, *Nature* **606**, 884 (2022).
- [30] C. E. Bradley, J. Randall, M. H. Abobeih, R. Berrevoets, M. Degen, M. A. Bakker, M. Markham, D. Twitchen, and T. H. Taminiau, A ten-qubit solid-state spin register with quantum memory up to one minute, *Physical Review X* **9**, 031045 (2019).
- [31] G. Van de Stolpe, D. Kwiatkowski, C. Bradley, J. Randall, M. Abobeih, S. Breitweiser, L. Bassett, M. Markham, D. Twitchen, and T. Taminiau, Mapping a 50-spin-qubit network through correlated sensing, *Nature Communications* **15**, 2006 (2024).
- [32] E. Moreva, E. Bernardi, P. Traina, A. Sosso, S. D. Tchernij, J. Forneris, F. Picollo, G. Brida, Ž. Pastuović, I. Degiovanni, *et al.*, Practical applications of quantum sensing: A simple method to enhance the sensitivity of nitrogen-vacancy-based temperature sensors, *Physical Review Applied* **13**, 054057 (2020).
- [33] E. H. Chen, H. A. Clevenson, K. A. Johnson, L. M. Pham, D. R. Englund, P. R. Hemmer, and D. A. Braje, High-sensitivity spin-based electrometry with an ensemble of nitrogen-vacancy centers in diamond, *Physical Review A* **95**, 053417 (2017).
- [34] C. S. Shin, C. E. Avalos, M. C. Butler, H.-J. Wang, S. J. Seltzer, R.-B. Liu, A. Pines, and V. S. Bajaj, Suppression of electron spin decoherence of the diamond nv center by a transverse magnetic field, *Physical Review B* **88**, 161412 (2013).
- [35] P. Jamonneau, M. Lesik, J. Tetienne, I. Alvizu, L. Mayer, A. Dréau, S. Kosen, J.-F. Roch, S. Pezzagna, J. Meijer, *et al.*, Competition between electric field and magnetic field noise in the decoherence of a single spin in diamond, *Physical Review B* **93**, 024305 (2016).
- [36] F. Dolde, H. Fedder, M. W. Doherty, T. Nöbauer, F. Rempp, G. Balasubramanian, T. Wolf, F. Reinhard, L. C. Hollenberg, F. Jelezko, *et al.*, Electric-field sensing using single diamond spins, *Nature Physics* **7**, 459 (2011).
- [37] K. R. K. Rao and D. Suter, Level anti-crossings of a nitrogen-vacancy center in diamond: decoherence-free subspaces and 3d sensors of microwave magnetic fields, *New Journal of Physics* **22**, 103065 (2020).
- [38] H. Clevenson, E. H. Chen, F. Dolde, C. Teale, D. Englund, and D. Braje, Diamond-nitrogen-vacancy electronic and nuclear spin-state anticrossings under weak transverse magnetic fields, *Physical Review A* **94**, 021401 (2016).
- [39] P. Lamba, A. Rana, S. Halder, S. Dhomkar, D. Suter, and R. K. Kamineni, Vector detection of ac magnetic fields by nitrogen vacancy centers of single orientation in diamond, *Physical Review B* **109**, 195424 (2024).
- [40] Z. Qiu, A. Hamo, U. Vool, T. X. Zhou, and A. Yacoby, Nanoscale electric field imaging with an ambient scanning quantum sensor microscope, *npj Quantum Information* **8**, 107 (2022).
- [41] N. Wang, C.-F. Liu, J.-W. Fan, X. Feng, W.-H. Leong, A. Finkler, A. Denisenko, J. Wrachtrup, Q. Li, and R.-B. Liu, Zero-field magnetometry using hyperfine-biased nitrogen-vacancy centers near diamond surfaces, *Physical Review Research* **4**, 013098 (2022).
- [42] J. R. Johansson, P. D. Nation, and F. Nori, Qutip: An open-source python framework for the dynamics of open quantum systems, *Computer Physics Communications* **183**, 1760 (2012).
- [43] To be precise, there is an anticrossing between the $I_z = +1$ and $I_z = -1$ components at $B_{\parallel} = 0$. This anticrossing is due to the orthogonal part of the hyperfine term. These states are very fragile, they are destroyed by an axial magnetic field around 100 nT and the energy gap created by the anticrossing is very small, around 2 kHz.

- [44] A. Dréau, M. Lesik, L. Rondin, P. Spinicelli, O. Arcizet, J.-F. Roch, and V. Jacques, Avoiding power broadening in optically detected magnetic resonance of single nv defects for enhanced dc magnetic field sensitivity, *Physical Review B* **84**, 195204 (2011).
- [45] R. Giri, F. Gorrini, C. Dorigoni, C. E. Avalos, M. Cazzanelli, S. Tambalo, and A. Bifone, Coupled charge and spin dynamics in high-density ensembles of nitrogen-vacancy centers in diamond, *Phys. Rev. B* **98**, 045401 (2018).
- [46] H. Babashah, H. Shirzad, E. Losero, V. Goblot, C. Galland, and M. Chipaux, Optically detected magnetic resonance with an open source platform, *SciPost Phys. Core* **6**, 065 (2023).
- [47] E. Bauch, S. Singh, J. Lee, C. A. Hart, J. M. Schloss, M. J. Turner, J. F. Barry, L. M. Pham, N. Bar-Gill, S. F. Yelin, *et al.*, Decoherence of ensembles of nitrogen-vacancy centers in diamond, *Physical Review B* **102**, 134210 (2020).
- [48] V. Dobrovitski, A. Feiguin, D. Awschalom, and R. Hanson, Decoherence dynamics of a single spin versus spin ensemble, *Physical Review B* **77**, 245212 (2008).
- [49] E. Bauch, C. A. Hart, J. M. Schloss, M. J. Turner, J. F. Barry, P. Kehayias, S. Singh, and R. L. Walsworth, Ultralong dephasing times in solid-state spin ensembles via quantum control, *Physical Review X* **8**, 031025 (2018).
- [50] The spectral width of $\frac{\pi}{2}$ pulse is approximately equal to the Rabi frequency of the MW.
- [51] N. Arunkumar, K. S. Olsson, J. T. Oon, C. A. Hart, D. B. Bucher, D. R. Glenn, M. D. Lukin, H. Park, D. Ham, and R. L. Walsworth, Quantum logic enhanced sensing in solid-state spin ensembles, *Physical Review Letters* **131**, 100801 (2023).
- [52] We are, again, neglecting the effect of the anticrossing.
- [53] N. Oshnik, P. Rembold, T. Calarco, S. Montangero, E. Neu, and M. M. Müller, Robust magnetometry with single nitrogen-vacancy centers via two-step optimization, *Physical Review A* **106**, 013107 (2022).
- [54] N. Arunkumar, K. S. Olsson, J. T. Oon, C. A. Hart, D. B. Bucher, D. R. Glenn, M. D. Lukin, H. Park, D. Ham, and R. L. Walsworth, Quantum logic enhanced sensing in solid-state spin ensembles, *Phys. Rev. Lett.* **131**, 100801 (2023).

Interplay between dressed and strong-axial field states in solid state spin ensembles-Supplementary Materials

G. Zanelli^{1,2}, E. Bernardi^{1*}, E. Moreva¹, E. Losero¹, S. Ditalia Tchernij^{2,3}, J. Forneris^{2,3}, Ž. Pastuović⁴, P. Traina¹, I. P. Degiovanni¹, M. Genovese^{1,3}.

¹*Istituto Nazionale di Ricerca Metrologica, Strada delle cacce 91, Turin, Italy**

²*Physics Department and NIS Centre of Excellence - University of Torino, Torino, Italy*

³*Istituto Nazionale di Fisica Nucleare (INFN) Sez. Torino, Torino, Italy and*

⁴*Centre for Accelerator Science, Australian Nuclear Science and Technology Organisation, New Illawarra rd., Lucas Heights, NSW 2234, Australia*

I. EXPERIMENTAL

A. Experimental Setup

The experimental setup is a single-photon sensitive confocal microscope in an inverted configuration. The excitation source is a 532 nm cw-laser (Prometheus 100NE), which can be pulsed using an acousto-optic modulator (Gooche & Housego 3080 – 125). The excitation is focused down to $\sim 2\mu\text{m}$ spot diameter onto the sample using an air objective (Olympus UPLANFL, 60x NA=0.67), which also collects the photoluminescence (PL) signal. The emitted PL is filtered with a 650 nm long-pass filter, and 10% of the emitted intensity is collected by a multi-mode optical fiber (core diameter = $50\mu\text{m}$) and recorded by a single photon avalanche photodiode (SPAD). The signal from the detector is recorded by a digital counter (Swabian Instruments Time Tagger 20) and sent to the software used for instrument control [1]. The MW signal required for ODMR is generated by an analog microwave generator (Keysight N5183B), then supplied to the power amplifier (SHL-16W-43-S+) using a switch (ZASW-2-50DRA+), which can be employed to pulse the signal using a pulse generator (Swabian Instrument Pulse Streamer 8/2). Finally, the mw is output to the sample using a planar antenna optimized to work efficiently around 2.87 GHz [2]. The bias magnetic field is supplied with a small magnet placed using a micro-manipulator and adjusted using a set of 3 Helmholtz coils. The sample is a $3 \times 3 \times 0.5$ mm CVD type IIa single-crystal diamond ($N < 1$ ppm, $B < 0.05$ ppm) from Element Six. NV centers have been created by 10 keV $^{14}\text{N}^+$ ion implantation with $F=1 \cdot 10^{14}\text{cm}^{-2}$ followed by a 2h thermal annealing @ 950°C . This processing yields a final concentration of NVs = $3 \cdot 10^{18}\text{cm}^{-3}$ (17 ppm) at a 10 nm depth from the surface while the concentration of residual substitutional nitrogen in the implanted region is $5.8 \cdot 10^{19}\text{cm}^{-3}$ (330 ppm).

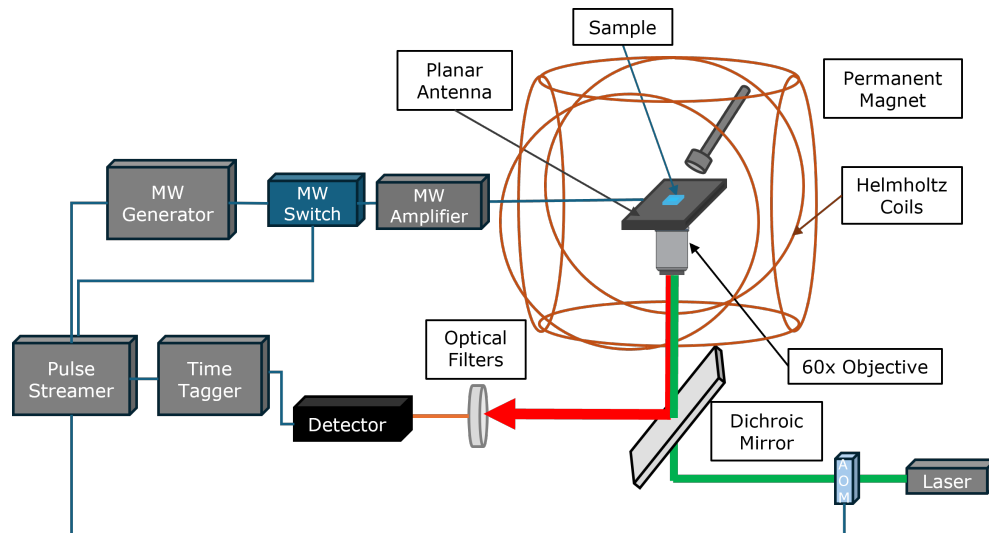


FIG. 1: figure
Experimental Setup

* e.bernardi@inrim.it

B. cw-ODMR and FID measurements parameters

Sample characterization has been carried out using two main techniques, namely, continuous-wave Optically Detected Magnetic Resonance (cw-ODMR) and Free Induction Decay (FID). The two techniques are based on the optical spin polarization induced on the NV center by laser irradiation (532 nm) and the application of a mw field to induce transitions between different spin sub-levels in the ground state. cw-ODMR former is characterized by a continuous application of initialization, driving and readout in the form of optical and microwave fields and presents an overall easier experimental implementation (Fig.2a). Conversely, the latter presents a sequence of pulses for initialization, driving and readout, rendering it more challenging to implement experimentally. The cw-ODMR measurements are performed applying continuously 5 mW of optical power, 30 mW of microwave power, for 10 minutes of measurement time. FID measurements are carried out for 120 minutes to acquire sufficient photon statistics to fit the experimental data. The different interval between pulses are reported in Table S.1, while the optical power is 20 mW and the microwave power is 10 W. The selection of initialization and readout pulse duration is strictly related to the optical power, as larger optical powers induce faster dynamics in the NV center [3]. Additionally, the time delay between initialization and readout laser pulses is kept constant to avoid drifts in the PL signal as the time τ between the mw pulses increases.

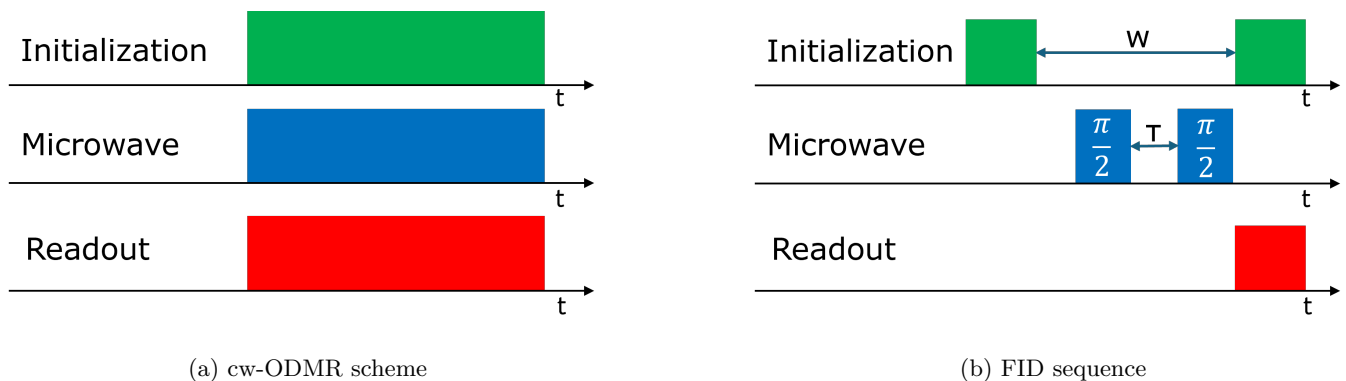


FIG. 2: (a) cw-Optically Detected Magnetic Resonance(ODMR) sequence (b) Free Induction Decay (FID) Sequence

Stage	Duration (μs)	cw-ODMR	FID
Initialization	∞		2.0
Readout	∞		1.5
Waiting time (w)	--		7.5
Dark Time	--		3

TABLE I: Sequence sections durations

II. CALCULATIONS OF STRAIN INSIDE BULK DIAMOND

The simulation of strain is conducted to obtain information about the relative orientation of strain with respect to the orthogonal field. This work is divided into 2 main sections: first, the calculation of the orientation of magnetic field performed using 3 orientations of NVs in high-field configuration, then, the orientation of strain with respect to the orthogonal field is computed by monitoring the effect on the NV orientation in orthogonal-field configuration.

A. Orientation of orthogonal field

The orientation and intensity of a 3D magnetic field can be obtained via vector magnetometry using an ensemble of NV centers. To perform this process, it is necessary to know the 4 orientations in space of the different NV families, knowing that the [100] orientation of the sample corresponds with the laboratory z-axis. The labels assigned to each family are the following:

The labels are then assigned to each cw-ODMR peak by recording subsequent spectra after adding a small axial field component ($B_{\parallel} \approx 0.5mT$) in each of the 4 different orientations respectively. The behavior of the spectroscopy lines can be easily computed via the Electron Zeeman term of the complete Hamiltonian:

$$H_{Zeeman} = -g_e \mu_B S \cdot B$$

where:

$$g_e : \text{electron gyromagnetic ratio} \quad \mu_B : \text{Bohr magneton}$$

$$S : \text{total spin} \quad B : \text{total magnetic field}$$

By monitoring the two peaks that exhibit the largest shifts at each step, it is possible to assign a crystallographic orientation to each peak:

NV Label	Crystallographic Orientation
NV_1	$[1\ 1\ 1]$
NV_2	$[1\ -1\ -1]$
NV_3	$[-1\ 1\ -1]$
NV_4	$[-1\ -1\ 1]$

TABLE II: Crystallographic orientation of the different NV families

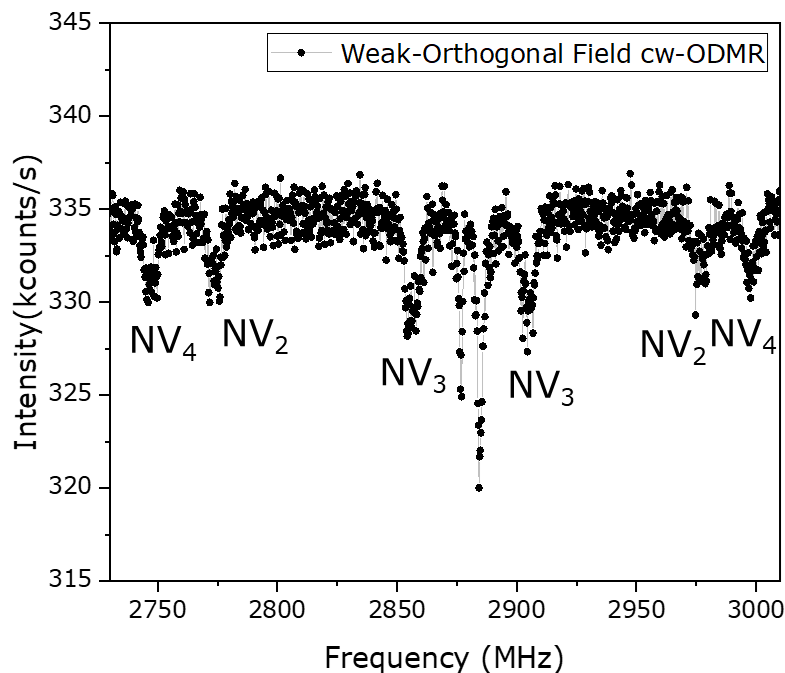


FIG. 3: Full range cw-ODMR

Once the peaks are labeled, it is now possible to obtain the direction of the orthogonal magnetic field in the reference frame of the NV_1 family. This is acquired by simulating the effect of a bias magnetic field rotating on the $[111]$ plane and then selecting the value where the spectroscopy lines of the NV_{2-3-4} families are ordered as in Fig. 3. Finally, the magnitude of the field is adjusted to fit the computed spectroscopy lines with the measured ones, yielding:

$$B_{\perp} = [3.86 - 3.29\ 0] mT$$

$$|B_{\perp}| = 5.07 mT, \phi_{B_{\perp}} = -40 \text{ deg}$$

B. Computation of strain components

The computation of strain components in the NV Hamiltonian is not straightforward, however if the orientation of the bias magnetic field is known, it is possible to reconstruct the strain using the lines from the NV_1 family (orthogonal field configuration):

$$-d_{\perp}[-\Pi_x(S_y^2 - S_x^2) + \Pi_y(S_x S_y + S_y S_x)] + d_{\parallel}[S_z^2 - \frac{1}{3}S(S+1)]$$

where:

$$\frac{d_{\perp}}{\hbar} = 17 \text{ Hz V}^{-1} \text{ cm}, \quad \frac{d_{\parallel}}{\hbar} = 0.35 \text{ Hz V}^{-1} \text{ cm}$$

Due to the larger coupling strength ($d_{\perp} \gg d_{\parallel}$), only the Π_x and Π_y components of strain are considered. The ϵ_{\perp} term can be computed easily from the zero field cw-ODMR as the frequency splitting follows [4]:

$$\Delta\omega_{\pm} = 2\epsilon_{\perp} = 2\sqrt{\Pi_x^2 + \Pi_y^2} \approx 5 \text{ MHz}$$

The value obtained will serve as a constraint for the evaluation of the magnitude of strain.

Starting from this, the electric field values obtained are: $\Pi_x = -133000 \text{ V cm}^{-1}$, $\Pi_y = 95000 \text{ V cm}^{-1}$. Finally, the relative angle between strain and orthogonal field is obtained from the complete numerical simulation as: $\phi_{\mathcal{E}} - \phi_{\mathcal{B}} = 175.5^\circ$, yielding $\phi_{\mathcal{E}} = 135.5^\circ$

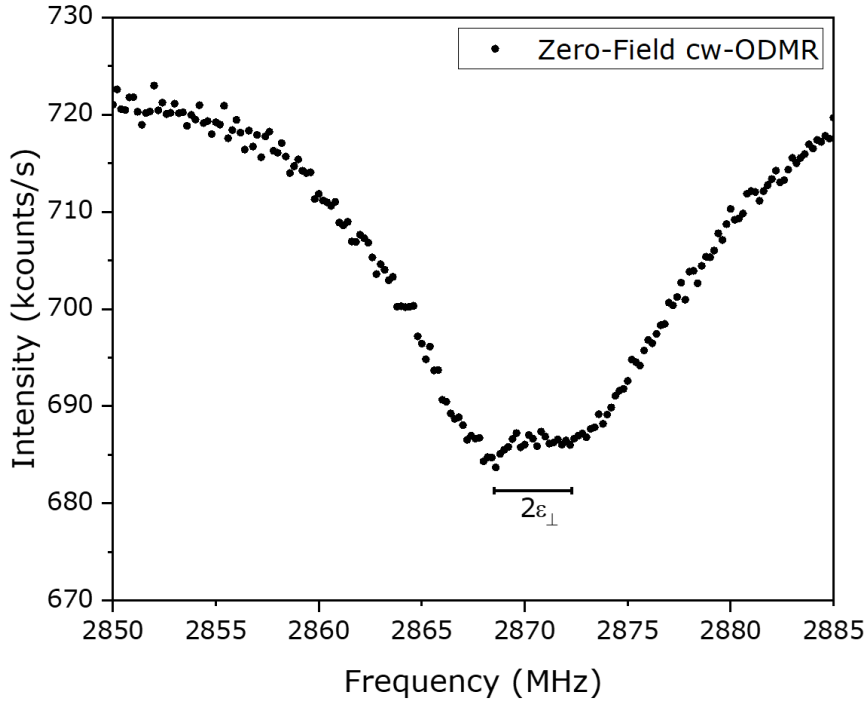


FIG. 4: Zero Field cw-ODMR

NV Center

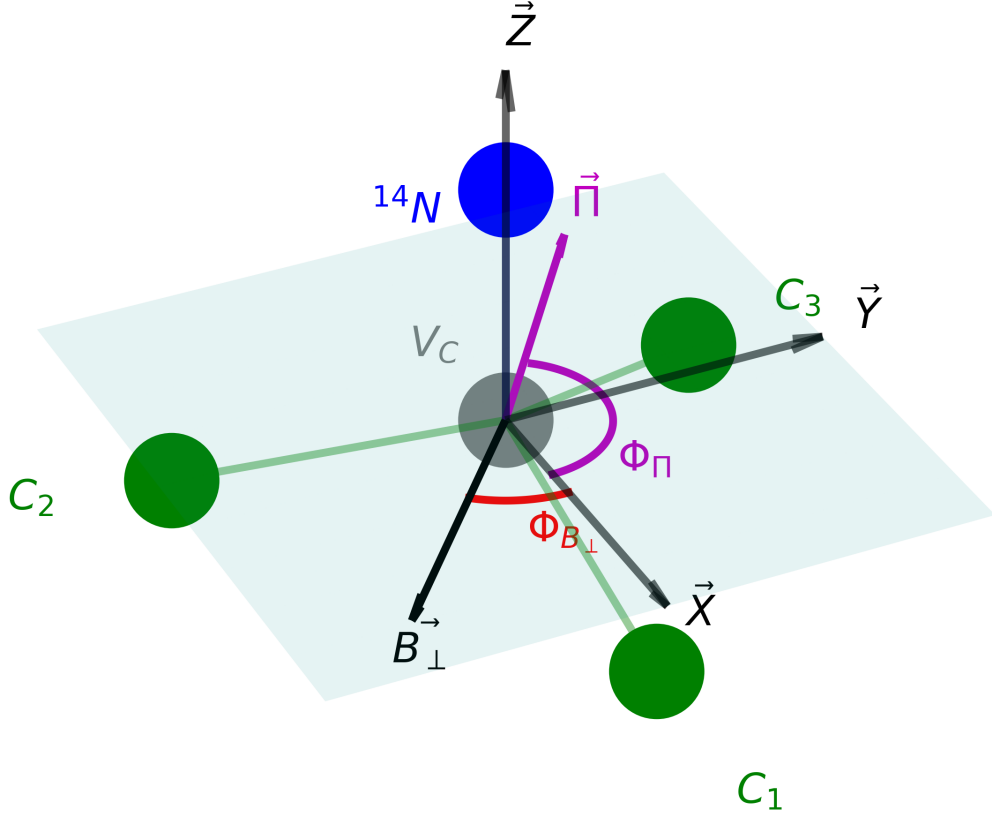


FIG. 5: Orthogonal field and strain relative orientations

III. COMPETITION BETWEEN ORTHOGONAL TOTAL ELECTRIC FIELD AND ORTHOGONAL MAGNETIC FIELD (EXACT SOLUTION)

A. Problem Set-up

We consider the Hamiltonian

$$\mathcal{H}_{elec-orth} = D_{gs} - d_\perp [\Pi_x (S_x S_y + S_y S_x) - \Pi_y (S_x^2 - S_y^2)] + g_e \mu_B B_x S_x + g \mu_B B_y S_y \quad (1)$$

where, as expressed in the main text, \vec{B} is the magnetic field and $\vec{\Pi} = \vec{E} + \vec{\sigma}$ is the total electric field that encompasses both the effect of static electric.

This hamiltonian can be expressed in the basis $|S_z = +1\rangle, |S_z = -1\rangle, |S_z = -1\rangle$ as

$$H_{elec-orth} = \begin{pmatrix} D_{gs} & \frac{\mathcal{B}_\perp [\cos(\phi_B) - i \sin(\phi_B)]}{\sqrt{2}} & -\mathcal{E} [\cos(\phi_\Pi) + i \sin(\phi_\Pi)] \\ \frac{\mathcal{B}_\perp [\cos(\phi_B) + i \sin(\phi_B)]}{\sqrt{2}} & 0 & \frac{\mathcal{B}_\perp [\cos(\phi_B) - i \sin(\phi_B)]}{\sqrt{2}} \\ -\mathcal{E} [\cos(\phi_\Pi) - i \sin(\phi_\Pi)] & \frac{\mathcal{B}_\perp [\cos(\phi_B) + i \sin(\phi_B)]}{\sqrt{2}} & D_{gs} \end{pmatrix} \quad (2)$$

where we introduced the following quantities:

$$\mathcal{B}_\perp = g\mu_B B_\perp, \quad \mathcal{E} = d_\perp \Pi_\perp \quad (3)$$

and

$$\phi_\Pi = \arctan\left(\frac{\Pi_y}{\Pi_x}\right), \quad \phi_{B_\perp} = \arctan\left(\frac{B_y}{B_x}\right) \quad (4)$$

B. Computation of eigenvalues

The eigenvalues of the Hamiltonian in Equation 1 are the values of λ for which the following system of equations admits not trivial solutions:

$$(H_{exact} - \lambda\mathbb{I}) \cdot \begin{pmatrix} a_1 \\ a_2 \\ a_3 \end{pmatrix} = \begin{pmatrix} 0 \\ 0 \\ 0 \end{pmatrix} \quad (5)$$

The condition of solubility:

$$\det(H_{exact} - \lambda\mathbb{I}) = 0 \quad (6)$$

leads to a cubic equation in λ . We found the three exact solutions of the cubic using the software Mathematica. The three exact solutions corresponds to the three exact eigenvalues $E_{0,exact}$, $E_{1,exact}$, $E_{2,exact}$.

To take into account the physics of the NV center, each eigenstate was written as a series expansion using $\zeta = \frac{\mathcal{B}_\perp}{D}$ as expansion parameter and $R = \frac{\mathcal{E}}{\mathcal{B}_\perp^2} = \frac{\mathcal{E}}{\zeta^2 D}$ as an ancillary parameter. Then only the terms till the second order in ζ were kept. The resulting approximated eigenvalues are:

$$\begin{aligned} E_0 &= -\frac{\mathcal{B}_\perp^2}{D_{gs}} \\ E_1 &= D_{gs} + \frac{\mathcal{B}_\perp^2}{D_{gs}} - 2 \left[\left(\frac{\mathcal{B}_\perp^2}{2D_{gs}} \right)^2 + \mathcal{E}^2 - \mathcal{E} \frac{\mathcal{B}_\perp^2}{D_{gs}} \cos(2\phi_{B_\perp} + \phi_\Pi) \right]^{\frac{1}{2}} \\ E_2 &= D_{gs} + \frac{\mathcal{B}_\perp^2}{D_{gs}} + 2 \left[\left(\frac{\mathcal{B}_\perp^2}{2D_{gs}} \right)^2 + \mathcal{E}^2 - \mathcal{E} \frac{\mathcal{B}_\perp^2}{D_{gs}} \cos(2\phi_{B_\perp} + \phi_\Pi) \right]^{\frac{1}{2}} \end{aligned} \quad (7)$$

These eigenvalues are the same as the one presented in ref. [5], a part a factor $\frac{1}{2}$ in first eigenvalue E_0 . We underline that the parameter R quantifies the relative strength of \mathcal{B}_\perp and \mathcal{E} . The choice of R expression was inspired by the fact that the term out of diagonal, like \mathcal{B}_\perp , appears at second-order in standard perturbation theory.

C. Computation of eigenstates

In order to find the eigenvector $|0\rangle$ corresponding to eigenvalue E_0 , first we found the expression of the general solution of 5, $(1, a_2(\lambda), a_3(\lambda))$, for a generic λ , where we set a_1 , i.e. the component parallel to $|S_z = 1\rangle$, equal to 1. Then we set $\lambda = E_{0,exact}$, we found the vector $|0\rangle_{exact} = (1, a_2(E_{0,exact}), a_3(E_{0,exact}))$ and we wrote each component of $|0\rangle_{exact}$ as a series expansion using ζ as expansion parameter and R as ancillary parameter. Lastly, only the terms till the first order ζ in $|0\rangle_{exact}$ were kept, giving $|0\rangle$. The same procedure was done for eigenvalues E_1 and E_2 resulting respectively in $|1\rangle$ and $|2\rangle$. The resulting eigenstates are

$$\begin{aligned}
|0\rangle &= \left(\frac{\mathcal{B}_\perp}{D_{gs}}, -\sqrt{2}e^{i\phi_{B_\perp}}, e^{i2\phi_{B_\perp}} \frac{\mathcal{B}_\perp}{D_{gs}} \right) \\
|1\rangle &= \left(1, \frac{1}{\sqrt{2}}e^{i\phi_{B_\perp}} \left(1 - \frac{1 - 2Re^{i(2\phi_{B_\perp} + \phi_\pi)}}{|1 - 2Re^{i(2\phi_{B_\perp} + \phi_\pi)}|^2} \right) \frac{\mathcal{B}_\perp}{D_{gs}}, -e^{i2\phi_{B_\perp}} \frac{1 - 2Re^{-i(2\phi_{B_\perp} + \phi_\pi)}}{|1 - 2Re^{-i(2\phi_{B_\perp} + \phi_\pi)}|^2} \right) \\
|2\rangle &= \left(1, \frac{1}{\sqrt{2}}e^{i\phi_{B_\perp}} \left(1 + \frac{1 - 2Re^{i(2\phi_{B_\perp} + \phi_\pi)}}{|1 - 2Re^{i(2\phi_{B_\perp} + \phi_\pi)}|^2} \right) \frac{\mathcal{B}_\perp}{D_{gs}}, e^{i2\phi_{B_\perp}} \frac{1 - 2Re^{-i(2\phi_{B_\perp} + \phi_\pi)}}{|1 - 2Re^{-i(2\phi_{B_\perp} + \phi_\pi)}|^2} \right)
\end{aligned} \tag{8}$$

It is interesting to discuss the limit case $R \ll 1$, i.e. when \mathcal{B}_\perp is predominant. In this case the eigenstates are

$$\begin{aligned}
|0\rangle &= \left(\frac{\mathcal{B}_\perp}{D_{gs}}, -\sqrt{2}e^{i\phi_{B_\perp}}, e^{i2\phi_{B_\perp}} \frac{\mathcal{B}_\perp}{D} \right) \\
|1\rangle &= (1, 0, -e^{i2\phi_{B_\perp}}) \\
|2\rangle &= \left(1, e^{i\phi_{B_\perp}} \frac{\mathcal{B}_\perp}{D_{gs}} \sqrt{2}, +e^{i2\phi_{B_\perp}} \right).
\end{aligned} \tag{9}$$

Collecting a global phase factor $e^{i\phi_{B_\perp}}$, we have:

$$\begin{aligned}
|0\rangle &= \left(e^{i\phi_{B_\perp}} \frac{\mathcal{B}_\perp}{D_{gs}}, -\sqrt{2}, e^{i\phi_{B_\perp}} \frac{\mathcal{B}_\perp}{D_{gs}} \right) = -\sqrt{2} \left(|S_z = 0\rangle - \frac{\mathcal{B}_\perp}{2D_{gs}} |+\rangle_{\phi_{B_\perp}} \right) \\
|1\rangle &= (e^{-i\phi_{B_\perp}}, 0, -e^{i\phi_{B_\perp}}) = \sqrt{2} |-\rangle_{\phi_{B_\perp}} \\
|2\rangle &= \left(e^{-i\phi_{B_\perp}}, \sqrt{2} \frac{\mathcal{B}_\perp}{D_{gs}}, +e^{i\phi_{B_\perp}} \right) = \sqrt{2} \left(|+\rangle_{\phi_{B_\perp}} + \frac{\mathcal{B}_\perp}{2D_{gs}} |S_z = 0\rangle \right)
\end{aligned} \tag{10}$$

where we introduced the vectors

$$\begin{aligned}
|-\rangle_{\phi_{B_\perp}} &= \frac{1}{\sqrt{2}} (e^{-i\phi_{B_\perp}}, 0, -e^{i\phi_{B_\perp}}) = \frac{1}{\sqrt{2}} (e^{-i\phi_{B_\perp}} |S_z = +1\rangle - e^{-i\phi_{B_\perp}} |S_z = -1\rangle) = Rot(\phi_{B_\perp}) |-\rangle \\
|+\rangle_{\phi_{B_\perp}} &= \frac{1}{\sqrt{2}} (e^{-i\phi_{B_\perp}}, 0, +e^{i\phi_{B_\perp}}) = \frac{1}{\sqrt{2}} (e^{-i\phi_{B_\perp}} |S_z = +1\rangle + e^{-i\phi_{B_\perp}} |S_z = -1\rangle) = Rot(\phi_{B_\perp}) |+\rangle
\end{aligned} \tag{11}$$

Considering Equations 9, it is clear that for $R \ll 1$ the effect of the orthogonal magnetic field is (i) to rotate the original dressed states $|-\rangle$ and $|+\rangle$ of angle ϕ_{B_\perp} equal to field orientation (ii) create a small mixing between $|+\rangle_{\phi_{B_\perp}}$ and $|S_z = 0\rangle$ states. These results are usually derived using second-order degenerate perturbation theory.

Now let's turn the attention to the general case $R \neq 0$. If we introduce the angle

$$\theta = \frac{1}{2} \arg \left(e^{i2\phi_{B_\perp}} \frac{1 - 2Re^{-i(2\phi_{B_\perp} + \phi_\pi)}}{|1 - 2Re^{-i(2\phi_{B_\perp} + \phi_\pi)}|^2} \right) = \frac{1}{2} \arg (e^{2i\phi_{B_\perp}} - 2Re^{-i\phi_\pi}) \tag{12}$$

,collecting a phase factor $e^{i\theta}$ Equations 8 can be written as

$$\begin{aligned}
|0\rangle &= e^{i(\phi_{B_\perp} - \theta)} \left(e^{-i\phi_{B_\perp}} \frac{\mathcal{B}_\perp}{D}, -\sqrt{2}, e^{i\phi_{B_\perp}} \frac{\mathcal{B}_\perp}{D} \right) = -\sqrt{2} e^{i(\phi_{B_\perp} - \theta)} \left(|S_z = 0\rangle - \frac{\mathcal{B}_\perp}{2D_{gs}} |+\rangle_{\phi_{B_\perp}} \right) = \\
&= -\sqrt{2} e^{i(\phi_{B_\perp} - \theta)} \left[|S_z = 0\rangle - \frac{\mathcal{B}_\perp}{2D_{gs}} (\cos(\phi_{B_\perp} - \theta) |+\rangle_\theta + i \sin(\phi_{B_\perp} - \theta) |-\rangle_\theta) \right] \\
|1\rangle &= \left(e^{-i\theta}, \sqrt{2} i \sin(\phi_{B_\perp} - \theta) \frac{\mathcal{B}_\perp}{D_{gs}}, -e^{i\theta} \right) = \sqrt{2} \left(|-\rangle_\theta + \frac{\mathcal{B}_\perp}{2D_{gs}} i \sin(\phi_{B_\perp} - \theta) |S_z = 0\rangle \right) \\
|2\rangle &= \left(e^{-i\theta}, \sqrt{2} \cos(\phi_{B_\perp} - \theta) \frac{\mathcal{B}_\perp}{D_{gs}}, -e^{i\theta} \right) = \sqrt{2} \left(|+\rangle_\theta + \frac{\mathcal{B}_\perp}{2D_{gs}} \cos(\phi_{B_\perp} - \theta) |S_z = 0\rangle \right)
\end{aligned} \tag{13}$$

The effect of orthogonal magnetic and electric field is to rotate the the original dressed states $|-\rangle$ and $|+\rangle$ of angle θ . As already said, $\theta = \phi_{B_\perp}$ for $R \ll 1$. On the other hand, $\theta = \frac{\pi}{2} - \frac{\phi_\Pi}{2}$ for $R \gg 1$, when the electric field is predominant [6]. This last point is in accord with eigenvalues present in ref. [5], if a global phase $-i$ is taken in account. The original result of this paper is the general expression of θ in equation 12, that states that for intermediate values of R , the competition between the orthogonal magnetic field B_\perp and the total electric field Π results in a intermediate rotation between ϕ_{B_\perp} and $\frac{\pi}{2} - \phi_\Pi/2$, determined on the relative magnitude of B_\perp and Π_\perp . Another result is that if $\mathcal{E} \neq 0$, $\theta \neq \phi_{B_\perp}$ and so both eigenvectors $|-\rangle_\theta$ and $|+\rangle_\theta$ are mixed with $|0\rangle$.

IV. EFFECT OF AN AXIAL MAGNETIC FIELD

We saw in the previous sections that the combined contribution of a total electric field and a weak orthogonal field can be summarized in three effects:

- Rotating the original dressed states $|S_z = 0\rangle, |-\rangle, |+\rangle$ of an angle θ along the z -axis, giving the eigenstates $|S_z = 0\rangle_\theta, |-\rangle_\theta, |+\rangle_\theta$. This is valid if we neglect the small mixing between $|-\rangle_\theta, |+\rangle_\theta$ and $|S_z = 0\rangle_\theta$
- Opening an energy gap between $|+\rangle_\theta$ and $|-\rangle_\theta$, $E_{gap} = 2 \left[\left(\frac{\mathcal{B}_\perp^2}{2D_{gs}} \right)^2 + \mathcal{E}^2 - \mathcal{E} \frac{\mathcal{B}_\perp^2}{D_{gs}} \cos(2\phi_{B_\perp}) \right]^{\frac{1}{2}}$
- Decrease the energy of the $|0\rangle$ state to $E_0 = -\frac{\mathcal{B}_\perp^2}{2D_{gs}} < 0$

We first consider negligible the mixing between $|-\rangle_\theta, |+\rangle_\theta$ and $|S_z = 0\rangle$. We can rewrite the Hamiltonian of the system as:

$$H_{B_z=0} = \begin{pmatrix} E_0 - E_m & 0 & 0 \\ 0 & -\frac{E_{gap}}{2} & 0 \\ 0 & 0 & +\frac{E_{gap}}{2} \end{pmatrix} \quad (14)$$

in the basis $|0\rangle_\theta, |-\rangle_\theta, |+\rangle_\theta$. We choosed $E_m = \frac{E_2 + E_1}{2} = D_{gs} + \frac{\mathcal{B}_\perp^2}{2D_{gs}}$ as the zero of the energy scale.

Following the derivation in present in Ref. [4], if we consider a magnetic field B_\parallel aligned along the NV axis, the total hamiltonian will be

$$H_{B_z \neq 0} = \begin{pmatrix} E_0 - E_m & 0 & 0 \\ 0 & -\frac{E_{gap}}{2} & \mathcal{B}_z \\ 0 & \mathcal{B}_z & +\frac{E_{gap}}{2} \end{pmatrix} \quad (15)$$

where $\mathcal{B}_\parallel = g\mu_B B_\parallel$. If we consider only the subspace $|-\rangle_\theta, |+\rangle_\theta$ the hamiltonian is

$$H_{red} = \begin{pmatrix} -\frac{E_{gap}}{2} & \mathcal{B}_\parallel \\ \mathcal{B}_\parallel & +\frac{E_{gap}}{2} \end{pmatrix} \quad (16)$$

If we now change the basis to $|S_z = -1\rangle_\theta, |S_z = +1\rangle_\theta$ we have:

$$H_{red} = \begin{pmatrix} -\mathcal{B}_\parallel & \frac{E_{gap}}{2} \\ \frac{E_{gap}}{2} & \mathcal{B}_\parallel \end{pmatrix} \quad (17)$$

This hamiltonian can be diagonalized exactly considering the system as one with effective spin $s = \frac{1}{2}$. The resulting eigenvectors will be:

$$\begin{aligned} |-\rangle_{\theta, \mathcal{B}_\parallel} &= \sin\left(\frac{\gamma}{2}\right) |S_z = +1\rangle_\theta - \cos\left(\frac{\gamma}{2}\right) |S_z = -1\rangle_\theta \\ |+\rangle_{\theta, \mathcal{B}_\parallel} &= \cos\left(\frac{\gamma}{2}\right) |S_z = +1\rangle_\theta + \sin\left(\frac{\gamma}{2}\right) |S_z = -1\rangle_\theta \end{aligned} \quad (18)$$

with $\tan \gamma = \frac{E_{gap}/2}{\mathcal{B}_\parallel}$.

The corresponding eigenenergies will be:

$$\begin{aligned}
E_{0'}^{(2)} &= -\frac{\mathcal{B}_\perp^2}{2D_{gs}} \\
E_{-, \theta, \mathcal{B}_\parallel}^{(2)} &= E_m - \sqrt{(E_{gap}/2)^2 + \mathcal{B}_\parallel^2} = D_{gs} + \frac{\mathcal{B}_\perp^2}{2D_{gs}} - \sqrt{(E_{gap}/2)^2 + \mathcal{B}_\parallel^2} \\
E_{+, \theta, \mathcal{B}_\parallel}^{(2)} &= E_m + \sqrt{(E_{gap}/2)^2 + \mathcal{B}_\parallel^2} = D_{gs} + \frac{\mathcal{B}_\perp^2}{2D_{gs}} + \sqrt{(E_{gap}/2)^2 + \mathcal{B}_\parallel^2}
\end{aligned} \tag{19}$$

It has to be underlined that the states $|-\rangle_{\theta, \mathcal{B}_\parallel}$, $|+\rangle_{\theta, \mathcal{B}_\parallel}$ are in general not balanced superposition of high field states $|S_z = +1\rangle, |S_z = -1\rangle$. The dependence of the coefficients of high field states as function of the axial field is shown in Figure 6 for the $|+\rangle_{\theta, \mathcal{B}_\parallel}$ where we consider $0 < \gamma < \pi$. For $\mathcal{B}_z = 0$, $\gamma = \frac{\pi}{2}$ and the coefficients are equal in modulus. Increasing \mathcal{B}_\parallel to higher positive values, $\gamma < \frac{\pi}{2}$ and the coefficient relative to the state $|S_z = +1\rangle$ became greater than the one relative to $|S_z = -1\rangle$. Decreasing \mathcal{B}_\parallel to lower positive values, the coefficient relative to the state $|S_z = -1\rangle$ became greater than the one relative to $|S_z = +1\rangle$. This exemplifies the changes from dressed states to partially dressed states and then to almost high-field states.

The expectation values of the axial spin are

$$\begin{aligned}
\theta, \mathcal{B}_\parallel \langle +|S_z|+\rangle_{\theta, \mathcal{B}_\parallel} &= \cos^2\left(\frac{\gamma}{2}\right) - \sin^2\left(\frac{\gamma}{2}\right) = \cos(\gamma) \\
\theta, \mathcal{B}_\parallel \langle -|S_z|-\rangle_{\theta, \mathcal{B}_z} &= \sin^2\left(\frac{\gamma}{2}\right) - \cos^2\left(\frac{\gamma}{2}\right) = -\cos(\gamma) \\
\langle 0|S_z|0\rangle_{\mathcal{B}_\parallel} &= 0.
\end{aligned} \tag{20}$$

From this expression follow that partially dressed states for opposite value of axial field B_\parallel have opposite value of $\langle S_z \rangle$ because $\cos(\frac{\pi}{2} - \gamma) = -\cos(\frac{\pi}{2} + \gamma)$, where, again, we recall that $\gamma = \frac{\pi}{2}$ for $\mathcal{B}_\parallel = 0$.

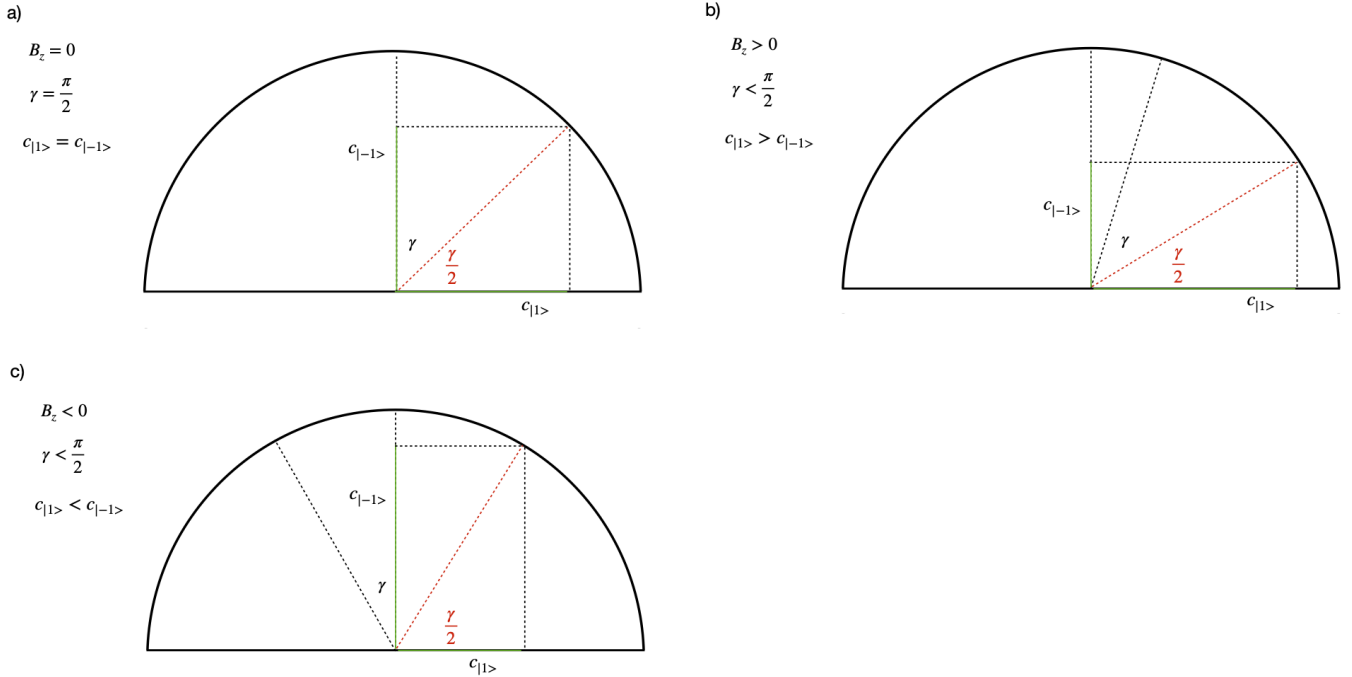


FIG. 6: Different balance of coefficients of high-field for a) $B_\parallel = 0$ b) $B_\parallel > 0$ c) $B_\parallel < 0$

Let's now consider also the mixing between $|-\rangle_\theta, |+\rangle_\theta$ and $|S_z = 0\rangle$. The basis to be considered is the one formed by the eigenvectors $|0\rangle, |1\rangle, |2\rangle$ in Equations 13. In this basis the total hamiltonian will be:

$$H_{B_z \neq 0} = \begin{pmatrix} E_0 - E_m & -\frac{\mathcal{B}_{\parallel}\mathcal{B}_{\perp}}{2D_{gs}} i \sin(\phi_{B_{\perp}} - \theta) & -\frac{\mathcal{B}_{\parallel}\mathcal{B}_{\perp}}{2D_{gs}} \cos(\phi_{B_{\perp}} - \theta) \\ -\frac{\mathcal{B}_{\parallel}\mathcal{B}_{\perp}}{2D_{gs}} i \sin(\phi_{B_{\perp}} - \theta) & -\frac{E_{gap}}{2} & \mathcal{B}_{\parallel} \\ -\frac{\mathcal{B}_{\parallel}\mathcal{B}_{\perp}}{2D_{gs}} \cos(\phi_{B_{\perp}} - \theta) & \mathcal{B}_{\parallel} & +\frac{E_{gap}}{2} \end{pmatrix} \quad (21)$$

Considering our experimental condition, $\frac{\mathcal{B}_{\parallel}\mathcal{B}_{\perp}}{2D_{gs}} i \sin(\phi_{B_{\perp}} - \theta) \ll E_0 - E_m = D_{gs} + \frac{\mathcal{B}_{\perp}^2}{D_{gs}}$ and we can consider the term $\frac{\mathcal{B}_{\parallel}\mathcal{B}_{\perp}}{2D_{gs}}$ as a perturbation of the hamiltonian in absence of mixing. Without going in detailed calculations, from perturbation theory we know that the effect of the perturbation will be of the order of $\frac{\mathcal{B}_{\parallel}^2\mathcal{B}_{\perp}^2}{D_{gs}^3}$ on the eigenergies and so we can consider it negligible.

V. POLARIZATION

This section will study how to excite dressed and partially dressed states using an oscillating magnetic field $B_{osc,x}$ with suitable polarization.

A. Dressed states

We consider the effect of an oscillating magnetic B_{osc} in driving the transition between the state $|0\rangle$ and dressed states $(|+\rangle_{\theta}, |-\rangle_{\theta})$. If the magnetic field is aligned along the direction defined by θ , $B_{osc} = \Omega (\hat{x} \cos \theta \cos(\omega_d t) + \hat{y} \sin \theta \cos(\omega_d t))$. The total time dependent Hamiltonian is

$$H_{0,dressed} = DS_z^2 + \Omega_{\theta} \cos(\omega_d t) (S_x \cos \theta + S_y \sin \theta) \quad (22)$$

For simplicity, we have considered only the part due to zero-field-splitting D . We move to the interaction basis defined by $H_0^{(1)} = \omega_d S_z^2$

$$H_{1,dressed} = U_0^{(1)}(t)^\dagger H_{0,dressed} U_0^{(1)}(t) - iU_0^{(1)}(t)^\dagger \partial_t U_0^{(1)}(t) \quad (23)$$

$$= \begin{bmatrix} D - \omega_d & \Omega e^{i\omega_d t} \cos(\omega_d t) (\cos \theta - i \sin \theta) & 0 \\ \Omega e^{i\omega_d t} \cos(\omega_d t) (\cos \theta + i \sin \theta) & 0 & \Omega (\cos \theta - i \sin \theta) e^{-i\omega_d t} \cos(\omega_d t) \\ 0 & \Omega e^{i\omega_d t} \cos(\omega_d t) (\cos \theta + i \sin \theta) & D - \omega_d \end{bmatrix} \quad (24)$$

$$\approx \begin{bmatrix} D - \omega_d & \Omega (\cos \theta - i \sin \theta) & 0 \\ \Omega (\cos \theta + i \sin \theta) & 0 & \Omega (\cos \theta - i \sin \theta) \\ 0 & \Omega (\cos \theta + i \sin \theta) & D - \omega_d \end{bmatrix} \quad (25)$$

$$= \begin{bmatrix} D - \omega_d & \Omega e^{-i\theta} & 0 \\ \Omega e^{+i\theta} & 0 & \Omega e^{-i\theta} \\ 0 & \Omega e^{+i\theta} & D - \omega_d \end{bmatrix} \quad (26)$$

$$(27)$$

Where $U_0^{(1)}(t) = \exp(-i\omega_d S_z^2)$, and we applied the rotating wave approximation, neglecting the terms rotating at $2\omega_d t$ in the second row. From the last row, is it clear that when B_{osc} is aligned with θ , it induce transition between $|0\rangle$ and $|+\rangle_{\theta}$. Similarly, it can be shown that when B_{osc} is aligned orthogonal to θ it induce transition between $|0\rangle$ and $|-\rangle_{\theta}$.

B. Partially Dressed states

Let's assume now an elliptically polarized mw excitation with the major axis aligned along θ :

$$B_{osc,x,y} = \Omega_{\theta} \cos(\omega_d t) (\hat{x} \cos \theta + \hat{y} \sin \theta) + \Omega_{\theta+\pi/2} \sin(\omega_d t) (\hat{x} \cos \theta + \hat{y} \sin \theta)$$

The total time dependent Hamiltonian is

$$H_{0,0,p-dressed} = DS_z^2 + \Omega_\theta \cos(\omega_d t) (S_x \cos \theta + S_y \sin \theta) + \Omega_{\theta+\pi/2} \sin(\omega_d t) (S_x \cos \theta + S_y \sin \theta) \quad (28)$$

also in this case, we have considered only the part due to zero-field-splitting D . We move to the interaction basis defined by $H_0^{(1)} = \omega_d S_z^2$

$$H_{1;dressed} = U_0^{(1)}(t)^\dagger H_{0,dressed} U_0^{(1)}(t) - iU_0^{(1)}(t)^\dagger \partial_t U_0^{(1)}(t) \quad (29)$$

$$= \begin{bmatrix} D - \omega_d \alpha & 0 \\ \beta & 0 & \alpha \\ 0 & \beta & D - \omega_d \end{bmatrix} \quad (30)$$

$$\approx \begin{matrix} D - \omega_d & \Omega_\theta (\cos \theta - i \sin \theta) + \Omega_{\theta+\pi/2} (\cos \theta + i \sin \theta) & 0 \\ \Omega_\theta (\cos \theta - i \sin \theta) - \Omega_{\theta+\pi/2} (\cos \theta + i \sin \theta) & 0 & \Omega_\theta (\cos \theta - i \sin \theta) + \Omega_{\theta+\pi/2} (\cos \theta + i \sin \theta) \\ 0 & \Omega_\theta (\cos \theta - i \sin \theta) - \Omega_{\theta+\pi/2} (\cos \theta + i \sin \theta) & D - \omega_d \end{matrix} \quad (31)$$

$$= \begin{bmatrix} D - \omega_d & \Omega_\theta e^{-i\theta} + \Omega_{\theta+\pi/2} e^{i\theta} & 0 \\ \Omega_\theta e^{-i\theta} - \Omega_{\theta+\pi/2} e^{i\theta} & 0 & \Omega_\theta e^{-i\theta} + \Omega_{\theta+\pi/2} e^{i\theta} \\ 0 & \Omega_\theta e^{-i\theta} - \Omega_{\theta+\pi/2} e^{i\theta} & D - \omega_d \end{bmatrix} \quad (32)$$

$$(33)$$

Where in the second row

$$\alpha = \Omega_\theta e^{i\omega_d t} \cos(\omega_d t) (\cos \theta - i \sin \theta) + \Omega_{\theta+\pi/2} e^{i\omega_d t} \sin(\omega_d t) (\sin \theta - i \cos \theta) \quad (34)$$

$$\beta = \Omega_\theta e^{i\omega_d t} \cos(\omega_d t) (\cos \theta + i \sin \theta) + \Omega_{\theta+\pi/2} e^{i\omega_d t} \sin(\omega_d t) (\sin \theta + i \cos \theta) \quad (35)$$

From the last row of Equation 33, it can be seen that the elliptically polarized mw excitation drive transition between $|0\rangle$ and $|+\rangle_{\theta, \mathcal{B}_\parallel}$ in Equation 18, if:

$$\sin\left(\frac{\gamma}{2}\right) = \Omega_\theta \quad (36)$$

$$\cos\left(\frac{\gamma}{2}\right) = \Omega_{\theta+\pi/2} \quad (37)$$

Summarizing, i) transition between $|0\rangle$ and dressed states are promoted by linearly polarized oscillating magnetic field, aligned along θ , i.e. along the direction determined by the competition between orthogonal magnetic field and total orthogonal electric field, or orthogonal to this direction ii) transition between $|0\rangle$ and partially dressed states are promoted by elliptically polarized oscillating magnetic field aligned or orthogonal to θ iii) Further more, it is well known that transition between $|0\rangle$ and strong axial field states are promoted by circularly polarized oscillating magnetic field [7].

VI. DECOHERENCE IN A FREE INDUCTION DECAY MEASUREMENT FOR A SINGLE NV CENTER

We use a derivation similar to the one presented in [4, 8–10]. We first consider the case of a single NV and then we discuss how to generalize the discussion to an ensemble of NV's.

The sources of decoherence for a single NV center are:

1. Coupling with ^{13}C
2. Coupling with ^{14}N or ^{15}N
3. Coupling with other spins
4. Temporal fluctuations of external fields

Decoherence due to the bath of surrounding spins, points 1-3 in the previous list, is a pure quantum phenomenon due to the entanglement of the NV center with the spin bath of surrounding —[10, 11]. For a limited class of problems, with so-called "nonbranching" evolution, we can map the original quantum spin bath onto a classical random magnetic field \vec{B}_{s-dec} [8]. We can consider that this field is aligned along the z-axis, $\vec{B}_{s-dec} = B_{s-random} \vec{z}$, because the orthogonal

part of this field is due to flip-flop terms in the spin-spin coupling and the flip-flop terms are suppressed by the big zero-field splitting D.

The temporal fluctuations of the external fields, point 4 in the previous list, can be described by two other stochastic magnetic B_{t-dec} and total electric fields Π_{t-dec} . Finally, we consider that the effect of the spin-spin coupling and of the temporal fluctuations adds up, giving a total stochastic magnetic field $\vec{B}_{dec} = B_{s-dec} + B_{t-dec}$.

For simplicity we consider B_{dec} and Π_{dec} have a gaussian distribution with zero mean and standard deviation σ_{B-dec_i} and $\sigma_{\Pi_{dec-i}}$, respectively on every cartesian components.

Fluctuations of the stochastic fields δB_{dec} and $\delta \Pi_{dec}$ induce fluctuations in the eigenenergies of the NV center and consequently fluctuations $\delta\nu$ in the ODMR transition frequencies. Fluctuations $\delta\nu$ in the ODMR transition will induce a decay in FID signal [4]. To fix the idea let's focus on the $|0\rangle \rightarrow |-\rangle_{B_z}$ ODMR transition. In general, the FID signal is proportional to the probability $p_{|0\rangle}$ to be in the $|0\rangle$

$$p_{|0\rangle}(\tau) = \frac{[1 - \cos(\phi + \delta\phi)]}{2} \quad (38)$$

where τ is the duration of the free precession interval, $\delta\phi = \int_0^\tau 2\pi\delta\nu dt$ and $\phi = 2\pi\Delta\tau$ are respectively the stochastic and static phase acquired during the free precession interval. $\Delta = \nu_{-B_z} - \nu_{MW}$ is the detuning between the microwave excitation frequency ν_{MW} and the ODMR transition. If we now consider the average on the different experimental realization

$$p_{FID}(\tau) = \langle p_{|0\rangle}(\tau) \rangle = \frac{[1 - e^{\langle \delta\phi^2 \rangle / 2} \cos 2\pi\Delta\tau]}{2} \quad (39)$$

we see that the FID decay is determined by the variance of stochastic phase acquired during the free precession interval, $\langle \delta\phi^2 \rangle$, where;

$$\langle \delta\phi^2 \rangle = 4\pi^2 \int_0^\tau dt \int_0^\tau dt' \langle \delta\nu(t)\delta\nu(t') \rangle. \quad (40)$$

So, now we have to study the correlation function $\langle \delta\nu(t)\delta\nu(t') \rangle$. To this end, we have to consider that :

1. δB_{dec} and $\delta \Pi_{dec}$ are random variables with correlations functions dacying exponentially.

$$\begin{aligned} \langle \delta B_{dec,i}(t)\delta B_{dec,i}(t') \rangle &= \sigma_{B_{dec,i}}^2 e^{|t-t'|/\tau_{c,B_{dec,i}}} \\ \langle \delta \Pi_{dec,i}(t)\delta \Pi_{dec,i}(t') \rangle &= \sigma_{\Pi_{dec,i}}^2 e^{|t-t'|/\tau_{c,\Pi_{dec,i}}} \end{aligned} \quad (41)$$

2. $\delta\nu_{res}$ dependence on δB_{dec} and $\delta \Pi_{dec}$ is set by the value of the static fields \vec{B} and $\vec{\Pi}$. Because, If $\sigma_{B_{dec,i}} = \sqrt{\langle \delta B_{dec,i}^2 \rangle} \ll B_i$ and $\sigma_{\Pi_{dec,i}} = \sqrt{\langle \delta \Pi_{dec,i}^2 \rangle} \ll \Pi_i, \forall i$, δB_{dec} and $\delta \Pi_{dec}$ act as perturbations on the eigenstates and eigenvalues set by \vec{B} and $\vec{\Pi}$ in the Hamiltonian in Eq. 21.

Now we will study the different scenarios set by the values of the static fields \vec{B} and $\vec{\Pi}$

A. Limit case: Small axial field

For the discussion, it's better to consider the quantities introduced before:

$$\mathcal{B}_\perp = \frac{g\mu_B}{h} B_\perp, \quad \mathcal{E} = d_\perp \Pi_\perp, \quad \mathcal{B}_z = \frac{g\mu_B}{h} B_z \quad (42)$$

If the condition

$$\sqrt{\mathcal{E}^2 + \frac{\mathcal{B}_\perp^2}{D_{gs}}} \gg \mathcal{B}_z \quad (43)$$

is fulfilled, the eigenstates are dressed states $|0\rangle, |+\rangle_\theta, |-\rangle_\theta$, where θ define two preferred direction x', y' in the plane orthogonal to NV-axis. Again we neglect the small mixing between $|+\rangle_\theta, |-\rangle_\theta$ and $|0\rangle$. The eigenenergies are $E_0, E_{+, \theta}, E_{-, \theta}$ with

$$E_{gap} = 2 \left[\left(\frac{\mathcal{B}_\perp^2}{2D_{gs}} \right)^2 + \mathcal{E}^2 - \mathcal{E} \frac{\mathcal{B}_\perp^2}{D_{gs}} \cos(2\phi) \right]^{\frac{1}{2}} \quad (44)$$

The fluctuations $\delta B_{dec,i}$ and $\delta \Pi_{dec,i}$ induce the following fluctuations in the eigenenergies, considering till the second order:

$$\begin{aligned} \delta E_{+, \theta} &= d_\perp \delta \Pi_{dec, y'} + \frac{(g\mu_B \delta B_{dec, z})^2}{E_{gap}} + \frac{(d_\perp \delta \Pi_{dec, x'})^2}{E_{gap}} + \\ &+ \frac{(g\mu_B \delta B_{dec, x'})^2}{D_{gs}} \\ \delta E_{-, \theta} &= -d_\perp \delta \Pi_{dec, y'} + \frac{(g\mu_B \delta B_{dec, z})^2}{E_{gap}} + \frac{(d_\perp \delta \Pi_{dec, x'})^2}{E_{gap}} + \\ &+ \frac{(g\mu_B \delta B_{dec, y'})^2}{D_{gs}} \\ \delta E_0 &= -\frac{(g\mu_B \delta B_{dec, x'})^2}{D_{gs}} - \frac{(g\mu_B \delta B_{dec, y'})^2}{D_{gs}} \end{aligned} \quad (45)$$

and, considering the $|0\rangle \rightarrow |-\rangle_\theta$ ODMR transition, we have the following expression for the fluctuation of the resonance frequency:

$$\delta \nu_- = \delta E_{-, \theta} - \delta E_0 = d_\perp \delta \Pi_{dec, y'} + \frac{(g\mu_B \delta B_{dec, z})^2}{E_{gap}} \quad (46)$$

where we neglected the term proportional to $\delta B_{dec, x'}$ because $D_{gs} \gg \mu_B \delta B_{dec, x'}$, and we neglected the term proportional to $\delta \Pi_{dec, x'}$ because we consider $\vec{\Pi}_{dec}$ isotropic.

It has to be underlined that the effect of fluctuations of the axial magnetic field δB_z is only at the second order, and it is scaled by the value of the energy gap E_{gap} . This is since $|-\rangle_\theta$ is a dressed state with $\langle S_z \rangle = 0$.

If we now consider a slowly fluctuating bath with $\tau \ll \tau_{c, B_{dec, z}}, \tau_{c, \Pi_{dec, y}}$, using the expression in Equation 46 through Equations 41 and 40, we can calculate the resulting variance of the phase fluctuation:

$$\langle \delta \phi^2 \rangle = 4\pi^2 \left[d_\perp^2 \sigma_{\Pi_{dec, y'}}^2 + \frac{(g\mu_B)^4 \sigma_{B_{dec, z}}^4}{E_{gap}^2} \right] \tau^2 \quad (47)$$

and so, from Equation 39, the FID decay:

$$p_{FID}(\tau) = \langle p|0\rangle(\tau) \rangle = \frac{\left[1 - e^{-\left(\frac{\tau}{T_2^*}\right)^2} \cos 2\pi \Delta \tau \right]}{2}, \quad (48)$$

with:

$$T_{2, dressed}^* = \frac{1}{\sqrt{2\pi}} \frac{1}{\sqrt{d_\perp^2 \sigma_{\Pi_{dec, y'}}^2 + \frac{(g\mu_B)^4 \sigma_{B_{dec, z}}^4}{E_{gap}^2}}}, \quad (49)$$

T_2^* define the characteristic time-scale of the FID decay. So, in this scenario, the more effective source of decoherence are the one related to $\Pi_{dec, y'}$, i.e. temporal fluctuations of the electrical fields or of the strain.

B. Limit case: strong axial field

If we now consider the condition

$$\mathcal{B}_z \gg \sqrt{\mathcal{E}^2 + \frac{\mathcal{B}_\perp^2}{D_{gs}}} \quad (50)$$

, the eigenstates in this case are strong-axial field states $|0\rangle, |S_z = +1\rangle, |S_z = -1\rangle$ with corresponding eigenenergies $E_0, E_{-1} = D_{gs} - g\mu_B B_z, E_{+1} = D_{gs} + g\mu_B B_z$. The fluctuations $\delta B_{dec,i}$ and $\delta \Pi_{dec,i}$ induce the following fluctuations in the eigenenergies, considering till the second order:

$$\begin{aligned} \delta E_{+1} &= g\mu_B \delta B_{dec,z} + \frac{d_\perp^2 (\delta \Pi_{dec,x'}^2 + \delta \Pi_{dec,y'}^2)}{2g\mu_B B_z} + \\ &+ \frac{1}{\sqrt{2}} \frac{(g\mu_B \delta B_{dec,x'})^2}{D_{gs} + g\mu_B B_z} + \frac{1}{\sqrt{2}} \frac{(g\mu_B \delta B_{dec,y'})^2}{D_{gs} - g\mu_B B_z} \\ \delta E_{-1} &= -g\mu_B \delta B_{dec,z} + \frac{d_\perp^2 (\delta \Pi_{dec,x'}^2 + \delta \Pi_{dec,y'}^2)}{2g\mu_B B_z} + \\ &+ \frac{1}{\sqrt{2}} \frac{(g\mu_B \delta B_{dec,x'})^2}{D_{gs} + g\mu_B B_z} + \frac{1}{\sqrt{2}} \frac{(g\mu_B \delta B_{dec,y'})^2}{D_{gs} - g\mu_B B_z} \\ \delta E_0 &= -\frac{(g\mu_B \delta B_{dec,x'})^2}{D_{gs} + g\mu_B B_z} - \frac{(g\mu_B \delta B_{dec,y'})^2}{D_{gs} - g\mu_B B_z} \end{aligned} \quad (51)$$

and, considering the $|0\rangle \rightarrow |-1\rangle$ ODMR transition, we have the following expression for the fluctuation of the resonance frequency:

$$\delta \nu_- = \delta E_{-1} - \delta E_0 = g\mu_B \delta B_{dec,z} + \frac{d_\perp^2 (\delta \Pi_{dec,x'}^2 + \delta \Pi_{dec,y'}^2)}{2g\mu_B B_z} \quad (52)$$

where we neglected the term proportional to $\delta B_{dec,x'}, \delta B_{dec,y'}$ because $D_{gs} \gg g\mu_B \delta B_{dec,x'}, g\mu_B \delta B_{dec,y'}$. In this scenario the effect of fluctuations of the axial magnetic field δB_z is at first order, instead the effect of the fluctuating total electric fields $\delta \Pi_x, \delta \Pi_y$ is at the second-order and it is scaled by $2g\mu_B B_z$. This is due to the fact that, in this scenario $\langle S_z \rangle = \pm 1$ for $|S_z = +1\rangle$.

Following the same line of reasoning of the previous section, it can be shown that the FID decay is characterized by a coherence time

$$T_{2,strongfield}^* = \frac{1}{\sqrt{2}\pi} \frac{1}{\sqrt{(g\mu_B)^2 \sigma_{B_{dec,z}}^2 + \frac{\sigma_{\Pi_{dec,x}}^4 + \sigma_{\Pi_{dec,y}}^4}{(2g\mu_B B_z)^2}}}, \quad (53)$$

So, in this scenario, the more effective source of decoherence are the one related to $B_{dec,z}$, i.e. the coupling with the different spin baths and the temporal fluctuations of the external magnetic field.

C. Limit case: Intermediate axial fields

If we now consider the condition

$$\mathcal{B}_z \sim \sqrt{\mathcal{E}^2 + \frac{\mathcal{B}_\perp^2}{D_{gs}}} \quad (54)$$

The eigenstates, in this case, are partially dressed states $|0\rangle, |-\rangle_{\theta, \mathcal{B}_z}, |+\rangle_{\theta, \mathcal{B}_z}$, see Equation 18. The fluctuations $\delta B_{dec,i}$ and $\delta \Pi_{dec,i}$ induce the following fluctuations in the eigenenergies, considering till the first order:

$$\begin{aligned}
\delta E_{+,\theta,B_z} &= g\mu_B \delta B_{dec,z} \cos(\gamma) + d_{\perp} \delta \Pi_{dec,y'} \sin(\gamma) \\
\delta E_{-,\theta,B_z} &= -g\mu_B \delta B_{dec,z} \cos(\gamma) - d_{\perp} \delta \Pi_{dec,y'} \sin(\gamma) \\
\delta E_0 &= -\frac{(g\mu_B \delta B_{dec,x'})^2}{D_{gs} + g\mu_B B_z} - \frac{(g\mu_B \delta B_{dec,y'})^2}{D_{gs} - g\mu_B B_z}
\end{aligned} \tag{55}$$

where $\tan(\gamma) = \frac{E_{gap}/2}{g\mu_B B_z}$ see Equations 19

It has to be underlined that in Eq. 55, the weights of $\delta B_{dec,z}$ and $\delta \Pi_{dec,y'}$ are set by the expectation value of $\langle S_z \rangle$ and $\langle S_x^2 - S_y^2 \rangle$, $\langle S_x S_y + S_y S_x \rangle$ on the eigenstates, for example $\langle +|S_z|+ \rangle_{B_z} = \cos(\gamma)$.

Considering the $|0\rangle \rightarrow |-\rangle_{\theta,B_z}$ ODMR transition, we have the following expression for the fluctuation of the resonance frequency:

$$\delta\nu_- = \delta E_{-,\theta,B_z} - \delta E_0 = -g\mu_B \delta B_{dec,z} \cos(\gamma) - d_{\perp} \delta \Pi_{dec,y'} \sin(\gamma) \tag{56}$$

Following the same line of reasoning of the previous sections, it can be shown that the FID decay is characterized by a coherence time

$$T_{2,partdressed}^* = \frac{1}{\sqrt{2\pi}} \frac{1}{\sqrt{(g\mu_B)^2 \sigma_{B-dec,z}^2 \cos^2(\gamma) + d_{\perp}^2 \sigma_{\Pi-dec,y'}^2 \sin^2(\gamma)}}. \tag{57}$$

So, in this scenario, both the sources related to $B - dec, z'$ and the one relates to $\Pi - dec, y'$ contribute to the decoherence. The relative weights of the different contributions depends on γ .

Summarizing:

- The FID decay is a stretched exponential with $p=2$
- The FID decay is characterized by a coherence time T_2^*
- The value of the static fields defines the effectiveness of the different sources of decoherence

VII. FREE INDUCTION DECAY MEASUREMENTS FOR STRONG AXIAL FIELD STATES

In this section, FID measurements recorded for the NV_2 family are reported. The B_{\parallel} component can be calculated from the full range cw-ODMR spectrum in Fig.3 yielding $B_{\parallel} \approx 3mT$.

The shorter T_2^* indicates the high-field character of the state (the complete list of T_2^* values can be found in Table 1 in the main text). The FID data was recorded by tuning the mw frequency in resonance with the central hyperfine peak, therefore only a single detuning ($\nu = 2.16 MHz$) is visible in the graph. As described in the previous section, strong-axial field states couple with the spin bath and fluctuations of external magnetic fields, leading to shorter coherence times with respect to dressed states, where the largest sources of decoherence are electric fields and strain fluctuations.

-
- [1] J. M. Binder, A. Stark, N. Tomek, J. Scheuer, F. Frank, K. D. Jahnke, C. Müller, S. Schmitt, M. H. Metsch, T. Uden, *et al.*, Qudi: A modular python suite for experiment control and data processing, *SoftwareX* **6**, 85 (2017).
- [2] K. Sasaki, Y. Monnai, S. Saijo, R. Fujita, H. Watanabe, J. Ishi-Hayase, K. M. Itoh, and E. Abe, Broadband, large-area microwave antenna for optically detected magnetic resonance of nitrogen-vacancy centers in diamond, *Review of Scientific Instruments* **87** (2016).
- [3] R. Giri, F. Gorrini, C. Dorigoni, C. E. Avalos, M. Cazzanelli, S. Tambalo, and A. Bifone, Coupled charge and spin dynamics in high-density ensembles of nitrogen-vacancy centers in diamond, *Physical Review B* **98**, 045401 (2018).
- [4] P. Jamonneau, M. Lesik, J. Tetienne, I. Alvizu, L. Mayer, A. Dréau, S. Kosen, J.-F. Roch, S. Pezzagna, J. Meijer, *et al.*, Competition between electric field and magnetic field noise in the decoherence of a single spin in diamond, *Physical Review B* **93**, 024305 (2016).
- [5] M. Doherty, F. Dolde, H. Fedder, F. Jelezko, J. Wrachtrup, N. Manson, and L. Hollenberg, Theory of the ground-state spin of the nv- center in diamond, *Physical Review B: Condensed Matter and Materials Physics* **85**, 205203 (2012).
- [6] We use the mathematical relation $\arg(-e^{i\phi}) = \pi + \phi$.

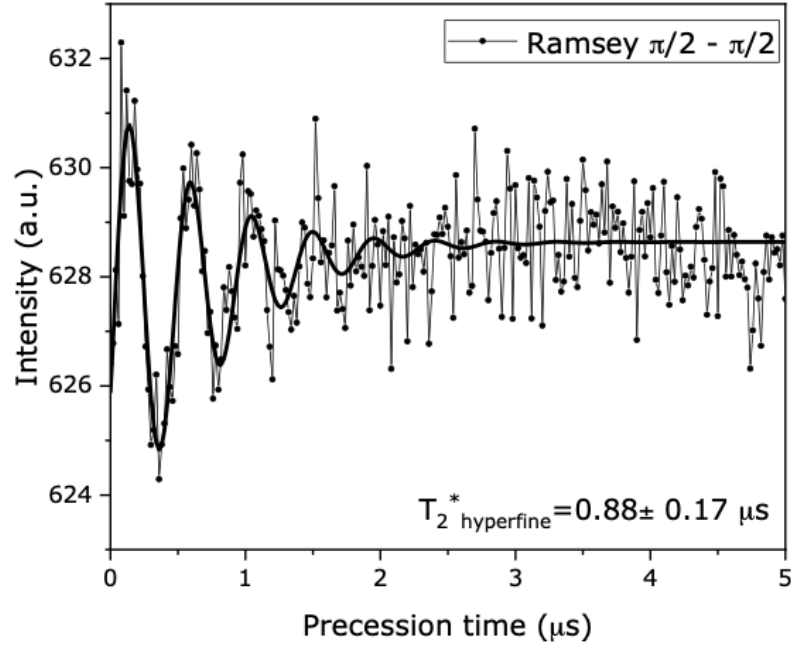


FIG. 7: FID relaxation for a microwave on resonance with the central peak of a hyperfine family at high fields

- [7] R. Pellicer-Guridi, K. Custers, J. Solozabal-Aldalur, A. Brodolin, J. T. Francis, M. Varga, A. Mongelos, J. Casanova, M. M. Paulides, and G. Molina-Terriza, Versatile quadrature antenna for precise control of large electron spin ensembles in diamond, *Advanced Quantum Technologies* , 2400142 (2024).
- [8] E. Bauch, S. Singh, J. Lee, C. A. Hart, J. M. Schloss, M. J. Turner, J. F. Barry, L. M. Pham, N. Bar-Gill, S. F. Yelin, *et al.*, Decoherence of ensembles of nitrogen-vacancy centers in diamond, *Physical Review B* **102**, 134210 (2020).
- [9] E. Bauch, C. A. Hart, J. M. Schloss, M. J. Turner, J. F. Barry, P. Kehayias, S. Singh, and R. L. Walsworth, Ultralong dephasing times in solid-state spin ensembles via quantum control, *Physical Review X* **8**, 031025 (2018).
- [10] V. Dobrovitski, A. Feiguin, D. Awschalom, and R. Hanson, Decoherence dynamics of a single spin versus spin ensemble, *Physical Review B* **77**, 245212 (2008).
- [11] W. H. Zurek, Decoherence, einselection, and the quantum origins of the classical, *Reviews of modern physics* **75**, 715 (2003).